# Chemical looping air separation with $Sr_{0.8}Ca_{0.2}Fe_{0.9}Co_{0.1}O_{3-\delta}$ perovskite sorbent: packed bed modeling, verification, and optimization

Runxia Cai [a], Jian Dou [a], Emily Krzystowczyk [a], Anthony Richard [b], Fanxing Li [a] *

[a] Department of Chemical and Biomolecular Engineering, North Carolina State University, 911 Partners Way, Raleigh, NC 27695-7905, USA

[b] Thermosolv LLC, 3474 N 3rd St, Laramie, WY 82072, USA

*E-mail: fli5@ncsu.edu

**Abstract:**

Chemical looping air separation (CLAS) represents a promising approach for efficient $O_2$ production from the air. The present study aims at optimizing the absorber/desorber operations and the separation process with extensive experimental validation. Specifically, a one-dimensional packed bed model was developed to investigate the CLAS operation with a $Sr_{0.8}Ca_{0.2}Fe_{0.9}Co_{0.1}O_{3-\delta}$ perovskite sorbent. The redox thermodynamics of perovskite sorbent was measured by TGA and then incorporated into a linear driving force model to describe the $O_2$ absorption and desorption rates. Both 4-step and 5-step air separation cycle configurations, with various cyclic structures, were performed in a subpilot-scale packed bed. The model predicted $O_2$ purity and productivity were consistent with experimental results, supporting its accuracy and applicability. Parametric analysis and multi-objective optimization were further carried out to assess the performance of CLAS. Both $O_2$ purity and recovery increased monotonically with the cycle time, airflow rate, steam flow rate, and absorption pressure. Meanwhile, optimal $O_2$ productivity and power consumption can only be achieved by specific combinations of these parameters. The optimized results showed that CLAS can be highly competitive when compared to conventional pressure swing adsorption (PSA) or cryogenic distillation. The 5-step cycle configuration achieved a minimum power consumption of 118 kW·h for producing 1 ton $O_2$ with ≥95% purity. The maximum $O_2$ productivity reached 0.0932 $g_{O2}/(g_{sorbent}\cdot h)$ with 390 kW·h/ton $O_2$ of energy consumption (95% pure). The optimization results also indicate that CLAS can potentially be more efficient than cryogenic distillation even when the required $O_2$ purity is above 99%.

**Keywords:**

Air separation; Perovskite; Modeling; Sorbent; Chemical Looping

## 1. Introduction

Oxygen ($O_2$) is an important industrial gas for chemical production, metallurgy, and power generation [1]. It also plays a crucial role in the medical sector [2]. Currently, $O_2$ is mainly produced from air separation [3]. Cryogenic distillation is the most mature and cost-effective air separation technology for producing large quantities of $O_2$ [4]. High purity $O_2$, nitrogen ($N_2$), and other byproducts can be separated by cooling and distillation based on boiling temperature differences among the gas products. However, this liquefaction process consumes a substantial amount of energy [5]. Even though many configurations have been proposed to improve the cryogenic air separation, the power consumption of state of the art still requires 200 kW·h/(ton $O_2$) to produce 97% pure $O_2$ and 300 kW·h/(ton $O_2$) to produce 99% pure $O_2$ [6-8]. Additionally, due to the high capital investment and the complex system design, cryogenic air separation is not suitable for applications that require fast startup/shutdown or consume small quantities of $O_2$ (e.g., less than several hundred tons/day) [9].

Besides cryogenic air separation, adsorption-based and membrane-based air separation technologies have also been extensively investigated [3]. Conventional adsorption technology accomplishes the air separation by physical adsorption of $N_2$ via pressure swing adsorption (PSA) or temperature swing adsorption (TSA). Zeolite-type sorbents, e.g., 5A, 13X, are the most widely used [10]. The adsorption-based technology, especially PSA, is ideal for small-scale operations that require fast startup and shutdown, such as the medical oxygen concentrator [11]. However, the insufficient selectivity of physical adsorption using zeolite

makes it difficult to completely separate $O_2$ from $N_2$, and this limits the $O_2$ purity to 90~95% for a single-stage PSA [12,13]. Moreover, the power consumption is very high (>500 kW·h/(ton $O_2$)) [14]. Multi-stage PSA can increase the $O_2$ purity to over 99%, but the process is even more energy-consuming, with $O_2$ recovery below 15% [15]. In addition, the amount of $N_2$ in the air is nearly four times that of $O_2$. As a result, large quantities of sorbents, which scale linearly with the oxygen production capacity, need to be used. This leads to larger bed sizes and higher capital costs. The large energy consumption and high capital cost make adsorption-based air separation economically unattractive for centralized applications. Polymer membranes and ion transport membranes are two other approaches for air separation [16,17]. Polymer membranes can produce concentrated $O_2$ with 60-80% purity but are not suitable for high purity $O_2$ production [18]. Ion transport membranes produce ultra-high purity $O_2$, but both the production capacity and the process efficiency are not competitive with other mature air separation technologies [19,20].

As a potentially efficient approach for oxygen generation, chemical looping air separation (CLAS) has attracted increased attention in recent years [21-23]. The operating modes of CLAS are similar to those of conventional adsorption-based systems, but it uses redox reactions of an oxygen sorbent for reversible oxygen release and uptake [24-26]. The oxidation of an oxide-based sorbent would absorb $O_2$ from the air at a low temperature and/or a high $O_2$ partial pressure, and the absorbed oxygen is subsequently released under a higher temperature and/or a lower $O_2$ partial pressure environment. The redox reactions are 100% selective for oxygen uptake and release. Therefore, high purity $O_2$ can be produced even with a simple cyclic configuration [27]. Moreover, the energy consumption of CLAS is expected

to be only 30%-50% of the advanced cryogenic air separation technology according to process simulation studies based upon Cu- and Mn-based oxygen sorbents [28,29]. However, a few practical limitations in heat exchange and reaction kinetics were not fully considered in these studies.

At present, there are two crucial aspects in the development of the CLAS technology: i). Development and optimization of oxygen sorbents; ii). Design and demonstration of the stable and high-efficiency system and process [30,31]. Extensive work has been performed for oxygen sorbent development, focusing primarily on improving sorbent activity, oxygen capacity, and long-term stability [32,33]. Copper oxide (CuO) and mixed transition metal oxides containing Mn and Co have been extensively investigated for both CLAS and chemical looping oxygen uncoupling (CLOU) [34-36]. They tend to exhibit high oxygen-carrying capacity but require very high operating temperatures ($\geq$ 800 $^{o}$C) [37,38]. The high operating temperature, however, negatively impacts the process efficiency, incurs high reactor cost, and leads to the sintering of metal oxides [39-41]. In comparison, perovskite-structured sorbents, particularly doped $SrFeO_3$, have shown promise for low temperature (400 – 650 $^{o}$C) operations [42-47].

Compared to the extensive research on oxygen sorbent development, relatively few studies have been devoted to process design for CLAS. Moreover, these studies mainly focused on simulating an interconnected fluidized beds configuration [29,48]. A pressure swing configuration, which is preferable in CLAS, is challenging to implement in the complex multi-fluidized bed systems [49,50]. Given the similarity between CLAS and nitrogen

sorbent-based PSA systems, detailed studies investigating CLAS reactor design, operating scheme, and performance with a packed bed absorber/desorber design are highly desirable. Specifically, numerical simulation can be an effective tool to design the PSA system and optimize operating parameters, such as cycle configuration, cycle time, adsorption and desorption pressures, and bed size [51-53]. Xu et al. [54] incorporated a first-order linear driving force (LDF) model into a one-dimensional (1D) model and simulated the CLAS process with $La_{0.1}Sr_{0.9}Co_{0.9}Fe_{0.1}O_{3-\delta}$ perovskite sorbent in a packed bed. However, due to lack of experimental data, the process simulation and optimization results have not been verified.

In this paper, a packed bed CLAS system using a $Sr_{0.8}Ca_{0.2}Fe_{0.9}Co_{0.1}O_{3-\delta}$ (SCFC8291) perovskite sorbent was simulated by accounting for oxygen non-stochiometry, redox kinetics, mass transfer, and heat transfer in a 1D numerical model. The simulation results were corroborated by experimental data from a subpilot-scale packed bed. Using the experimentally validated numerical model, the cycle configuration, cycle time, air flow rate, steam flow rate, absorption pressure were systematically studied to evaluate their impacts on $O_2$ purity, productivity, and recovery, as well as power consumption. The $O_2$ productivity and power consumption Pareto fronts and the $O_2$ purity and power consumption Pareto fronts were obtained by multi-objective optimization. The results showed that CLAS can be highly competitive compared to existing approachs. The 5-step cycle configuration achieved a minimum power consumption of 118 kW·h for producing 1 ton $O_2$ with $\geqslant$95% purity, and the maximum $O_2$ productivity reached 0.0932 $g_{O2}/(g_{sorbent}\cdot h)$ with 390 kW·h/(ton $O_2$). The findings also indicate that CLAS can be more efficient than cryogenic distillation even when the required $O_2$ purity is above 99%.

## 2. Experimental and simulation methods

### 2.1. Material preparation and characterization

A 1 kg batch of SCFC8291 sorbent was synthesized by using the sol-gel method. This method produced oxygen sorbent with faster kinetic rate and higher oxygen capacity compared to samples prepared by solid-state reaction or co-precipitation method in our previous study [55]. We note that oxygen capacity was measured by pressure swing between 2 min of Ar flow and 1 min of 20% $O_2$ flow so the measured oxygen capacity was affected by both redox kinetics and thermodynamics. In addition, the oxygen vacancy concentrations can also be affected by the synthesis methods [56].

Stoichiometric mixtures of $Sr(NO_3)_2$, $Ca(NO_3)_2{\cdot}4H_2O$, $Fe(NO_3)_3{\cdot}9H_2O$, and $Co(NO_3)_2{\cdot}6H_2O$ were dissolved in the deionized water. 5 mole citric acid per mole of sorbent was then added into the solution at room temperature under vigorous stirring for 30 min. After that, 7.5 mole ethylene glycol per mole of sorbent was added to the solution and followed by stirring at 80$^{o}$C for three hours to form a gel-like mixture. The resulting composite was dried at 120 $^{o}$C overnight and heated at 1100 $^{o}$C in the air for 10 h to eliminate the organic contents. After cooling down to room temperature, the sorbent was reheated to 1100 $^{o}$C and isothermal for another 10 h to remove any impurity and form the pure perovskite phase. The samples were grounded into powders and then compressed into the cylindrical pellet with 3 mm in diameter and 12 mm in length by a pellet extruder. The resulting pellets were sintered at 950 $^{o}$C for 60 h and then slowly ramped down to room temperature with 100

°C/h.

X-ray diffraction of SCFC8291 powders was conducted on an Empyrean PANalytical XRD with Cu Kα radiation (λ=1.5406 Å) at 45 kV and 40 mA. The scanning range of 2θ was from 15° to 80° with a step size of 0.026°. As shown in Fig. S1, the XRD pattern of SCFC8291 shows a pure perovskite phase.

2.2. TGA experiment

The oxygen non-stoichiometry of SCFC8291 at different $O_2$ partial pressures and temperatures were measured using a Thermal Gravimetric Analyzer (TGA, TA-Instrument SDT Q650). 50 mg sample was grounded into fine particles with size smaller than 90 μm and then loaded into a 70 μL alumina crucible. The $O_2$ volume fraction varied from 0.2% to 50%, and the total gas flow rate was maintained at 200 ml/min. All mass flow controllers were calibrated by the Definer 220 volumetric flow meter before experiments. The $O_2$ concentrations above 1 vol. % was adjusted by mixing the pure $O_2$ (Airgas extra dry grade $O_2$) with the pure argon (Airgas UHP 5.0 grade Ar), while those concentrations below 1 vol.% were achieved by replacing pure $O_2$ with 1.048 vol.% $O_2$ calibration gas (Airgas argon balance). The temperature was increased from room temperature to 650 °C under the 50 % $O_2$ atmosphere and then was isothermal for 10 min until no further weight change was observed. After that, the temperature was ramped down to 625°C and held for a specific time. The non-stoichiometric values at 600 °C, 575 °C, and 550 °C were also obtained by the same program. Then, the temperature was increased to 650 °C again, and the next cycle of the

temperature test was started under a different $O_2$ concentration. The increase and decrease rates of the temperature were all 20 $^oC$/min. After all temperatures and $O_2$ concentrations were measured, the temperature was raised to 1100 $^oC$. The SCFC8291 samples were held in the 20% $H_2$ atmosphere for 30 min to be entirely reduced to a mixture of SrO, CaO, Fe, and Co. With this reference point, the non-stoichiometry at different conditions can be calculated by Eq.(1). Four more repeated experiments were conducted to verify the reproducibility and obtain the error bar.

$$\delta = 2 - \frac{m_s - m_{reduced}}{MW_O} \cdot \frac{MW_{reduced}}{m_{reduced}} \quad (1)$$

2.3. Packed bed experiment

The schematic diagram of the packed bed experimental system is shown in Fig. 1. The packed bed reactor is a vertical stainless steel tube with a 0.0206 m inner diameter. 357.63 g of pellets were loaded into the reactor, and the apparent packing density was about 1.83 g/cm$^3$. The pellets were closely packed at the bottom part of the packed bed, so the dead volume in the upstream (bottom) part can be neglected. The dead volume in the downstream part needs to be estimated by experiments. The bed temperature was measured using a thermocouple placed at a distance of ~50 cm from the bed inlet. Six other thermocouples embedded in the refractory were used to monitor and control the furnace temperatures. The pressure was measured using pressure transducers, and the $O_2$ concentrations were measured using an $O_2$ analyzer. Data were collected each second and logged on the computer. Before the breakthrough experiment, the bed column was held under ~900 Pa vacuum for 10 min and

then purged with 1 standard liter per minute (SLM) $N_2$ (99.9% purity) for about 20 min at ambient pressure until the $O_2$ concentration was below 0.1%. This pretreatment process was only used in the breakthrough experiment. After that, the packed bed was swept by 1 SLM synthetic air (20.9% $O_2$) at 246.5 kPa for 2000 s until the $O_2$ concentration in the outflow stream reached 20.9%. The inlet gas temperature and the furnace temperature were all maintained at 600 $^oC$, nominally.

The basic 4-step cycle configuration for PSA by zeolite often consists of a pressurization step, a high-pressure adsorption step, a depressurization step, and a low-pressure desorption step [57]. More complex cycle configurations, which contain the purge step, the vacuuming step, or some other processes, are mainly for achieving higher $O_2$ purity, lower power consumption, or some other objectives [58]. Therefore, two cycle configurations were designed for CLAS experiments with SCFC8291 sorbents in this paper. A 4-step cycle configuration was used as the basic configuration. 1~3 SLM air flowed into the packed bed from the upstream. The downstream pressure was controlled by a back pressure regulator (BPR) and raised to about 280 kPa. The pressurization step took about 4 seconds and was followed by a specific time of absorption. After the absorption process, the upstream air flow was stopped, and the pressure was released to nearly ambient pressure. This depressurization step lasted 5 seconds. Then, the counter-current desorption step started under 110 kPa by using steam. The mixture gas was passed through the condenser to remove water vapor, and the $O_2$ product was collected in the product tank. Afterward, it took 1 second to stop the steam injection, and then the next cycle started. For each experimental condition, the packed bed system was continuously operated for many cycles. The $O_2$ concentration in the product

stream was also continuously monitored. If the curves of $O_2$ concentration in two consecutive cycles remained almost unchanged, the system was considered to have reached the pseudo-steady-state, and then ten continuous cycles were carried out to obtain stable performance of $O_2$ production. In the 5-step cycle configuration, a recycle step was added after the depressurization step to enhance the $O_2$ purity. $O_2$ product was collected and stored in a reservoir. 1.4 SLM of $O_2$-enriched gas was extracted from the reservoir in the recycle step and then pumped back to the packed bed under ambient pressure. Part of the $N_2$ in the bed voidage and the dead volume was removed so the $O_2$ purity could be increased. All experiments were carried out at 600 °C.

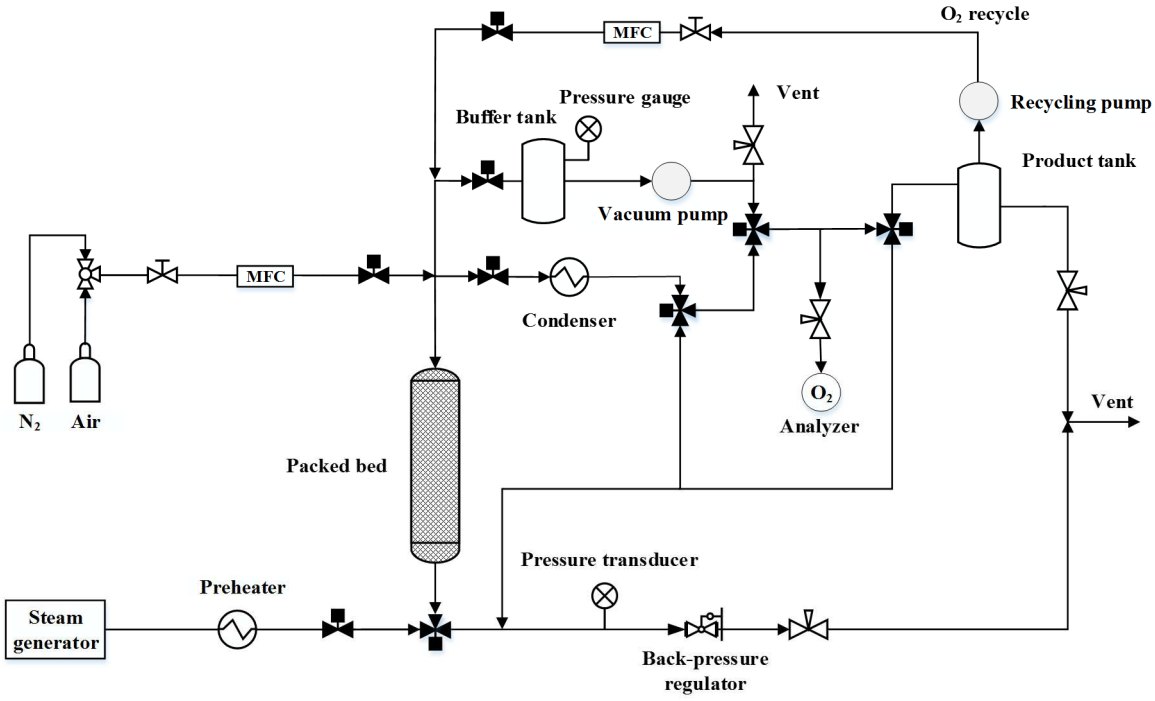


Fig. 1 Schematic diagram of the CLAS experimental system

## 2.4. Model description

One-dimensional (1D) models have been widely accepted for calculating the adsorption

process in the packed bed owing to its reasonable accuracy and less computational cost [59-62]. Therefore, it is adopted for simulating the CLAS process in the current study. The oxidation and reduction kinetics of perovskite-type sorbents in a TGA have been described by different models in literature [63-66]. In terms of the mass transfer conditions and adsorption behaviors in the packed bed, the first-order LDF model is the most common model for calculating PSA by zeolite. The first-order LDF model was also adopted and then verified in the paper. The following assumptions are employed:

1. The radial gradients of temperature, pressure, concentration, and velocity are neglected.
2. The momentum balance is described by the Ergun equation.
3. Compressed air is considered as a mixture of $N_2$ and $O_2$ with a volumetric ratio of 79.1:20.9. Other minor impurities are neglected.
4. The ideal gas law is applicable for all three gas components ($O_2$, $N_2$, and $H_2O$).
5. The external and internal mass transfers of $O_2$ follow the first-order LDF model, and lump coefficients were fitted to describe the $O_2$ absorption and desorption rates.
6. The system is non-isothermal, but the gas and solid phases are in thermal equilibrium.
7. The particle size and the bed voidage are uniform along the packed bed.
8. The temperature of the inner surface of the packed bed column remains constant.
9. The variation of steam flow rate is neglected in the 1s valve-closing step. Steam injection is assumed to remain unchanged for 1s until an instantaneous stop at the end of the step. Therefore, the desorption step and the valve-closing step in the experiments are combined as the desorption step in the model.

Two configurations were simulated based on the aforementioned experiments. The basic 4-step configuration consisted of (1) pressurization with air feed (PR); (2) absorption with air feed (AB); (3) co-current depressurization (DP); (4) counter-current desorption with steam injection (DE). The 5-step cycle configuration included an additional oxygen recycle (RE) step, between depressurization and desorption steps, to purge out $N_2$ in the particle interstices and the dead volume to improve the $O_2$ purity. The fraction of the recycled $O_2$ was determined based on the $O_2$ product obtained in the previous cycle. The 4-step and 5-step cycle configurations are shown in Fig. 2.

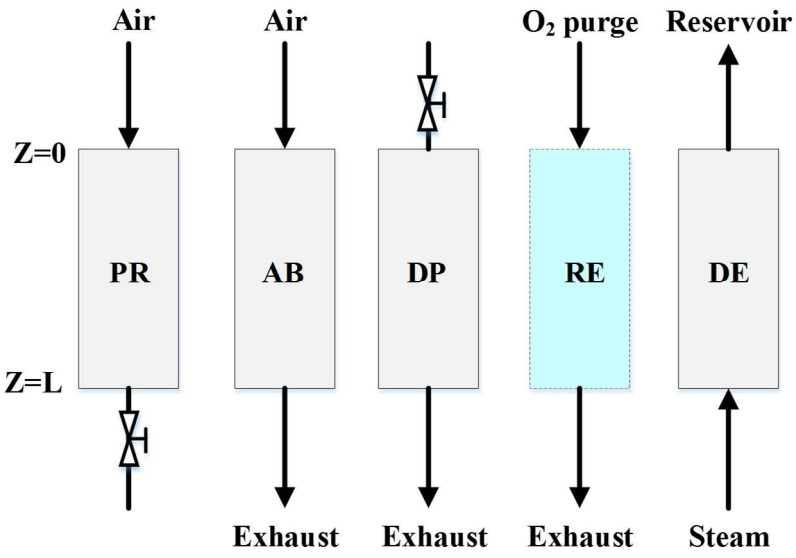


Fig. 2 Schematics of the 4-step cycle configuration (including PR, AB, DP, and DE) and the 5-step cycle configuration (including PR, AB, DP, RE, and DE)

2.5. Mathematical equations

Based on the above assumptions, the mass conservation equation of each gas component

can be described by Eq.(2):

$$\varepsilon_b \frac{\partial C_i}{\partial t} + \rho_b \frac{\partial q_i}{\partial t} = -\frac{\partial (uC_i)}{\partial z} + \varepsilon_b \frac{\partial}{\partial z}\left( D_{z,i} \frac{\partial C_i}{\partial z} \right) \quad i = 1, 2, 3 \tag{2}$$

The absorption amount on perovskite sorbents is neglected for $N_2$ and steam.

The axial mass dispersion coefficients can be calculated by Eq.(3) [67]:

$$D_{z,i} = 0.73 D_{m,i} + \frac{0.5 u d_p / \varepsilon_b}{1 + 9.7 \frac{D_{m,i}}{u d_p / \varepsilon_b}} \tag{3}$$

The momentum balance can be described by the Ergun equation:

$$\frac{\partial P}{\partial z} = -\frac{150 \mu_g (1-\varepsilon_b)^2}{d_p^2 \varepsilon_b^3} u - \frac{1.75(1-\varepsilon_b)}{d_p \varepsilon_b^3} \rho_g u^2 \tag{4}$$

The energy balance can be calculated by Eq.(5)

$$\left(\varepsilon_b \rho_g c_{pg} + \rho_b (1-\varepsilon_b) c_{ps}\right) \frac{\partial T}{\partial t} + \frac{1}{2} \rho_b \Delta H_{ad,O_2} \frac{\partial q_i}{\partial t} - \varepsilon_b \frac{\partial P}{\partial t} = -\frac{\partial (u \rho_g c_{pg} T)}{\partial z} + \varepsilon_b \frac{\partial}{\partial z}\left( \lambda_{eff} \frac{\partial T}{\partial z} \right) + \frac{4U}{D_t}(T_w - T) \tag{5}$$

The heat capacity of $SrFeO_{2.5}$ at 600 °C was used as a substitution for that of SCFC8291 [68]. As the heat capacity of the solid material dominates the heat transfer in a particle, the heat release and absorption of gas inside a particle were neglected in the energy balance equation.

The absorption of $O_2$ is exothermic and desorption is endothermic. The absorption enthalpy at different non-stoichiometric values can be obtained by Van't Hoff equation [69]:

$$\ln\left(\frac{P_{O_2}}{P^0}\right)=-\frac{\Delta H_{ab,O_2}(\delta)}{RT}+\frac{\Delta S_{ab,O_2}(\delta)}{R} \tag{6}$$

The corresponding $\Delta H_{ab,O_2}$ was fitted by using an empirical Eq.(7). As shown in Fig. S2, the calculation results matched up well with the experimental data within the range of δ=0.26-0.50.

$$\Delta H_{ab,O_2}(\delta)=457580\times\delta^4-681302\times\delta^3+370726\times\delta^2-86405\times\delta+7089.7 \tag{7}$$

The absorption and desorption rates of sorbents are described by the first-order LDF model.

$$\frac{\partial q_{O_2}}{\partial t}=k_{LDF}\left(q^*_{O_2}-q_{O_2}\right) \tag{8}$$

$k_{\mathrm{LDF}}$ are specified as $k_{\mathrm{AB}}$ for the absorption step and $k_{\mathrm{DE}}$ for the desorption step in the following sections. For the perovskite, the $O_2$ absorption amount can be explicitly described by the $O_2$ non-stoichiometry at a specific state and the reference state.

$$q_{O_2}=\frac{\delta-\delta_0}{2MW_s} \tag{9}$$

Then, Eq.(10) can be obtained by incorporating Eq.(9) into Eq.(8).

$$\frac{\partial q_{O_2}}{\partial t}=\frac{1}{2MW_{\mathrm{s}}}\frac{\partial\delta}{\partial t}=\frac{1}{2MW_{\mathrm{s}}}k_{LDF}\left(\delta^*-\delta\right) \tag{10}$$

The initial and boundary conditions are listed in Table 1 [70]. The inlet gas velocities at the PR step and the outlet gas velocities at the DP step were estimated by using the valve

equations.

$$u_{valve} = C_v \frac{4R}{\varepsilon_b \pi D_t^2} \sqrt{\frac{T}{MW_g}} 1.179 \sqrt{\frac{\left(P_{high}^2 - P_{low}^2\right)}{P^2}}, \ if \ P_{low} > 0.53 P_{high}$$
$$u_{valve} = C_v \frac{4R}{\varepsilon_b \pi D_t^2} \sqrt{\frac{T}{MW_g}} \cdot \frac{P_{high}}{P}, \quad if \ P_{low} \le 0.53 P_{high} \tag{11}$$

If the gas stream is leaving the bed, P equals $P_{high}$. If the gas stream is entering the bed, P equals $P_{low}$ [70]. The coefficients ($C_v$) for both PR and DP steps were fitted based on the experimental pressure curves. As shown in Fig. S3, the predictive pressure curves matched well with the experimental results of a typical 4-step cycle configuration.

Table 1 Initial and boundary conditions for 1D model

| Initial conditions:<br>$C(O_2)= 10^{-3}C_0$; $C(H_2O)= 10^{-5}C_0$; $C(N_2)= C_0- C(O_2)- C(H_2O)$;<br>$T_0=T_{in}$, $P_0=101325$Pa, $\delta_0=\delta(P(O_2), T_{in})$ | | |
|---|---|---|
| Step | Z=0 (inlet) | Z=L (outlet) |
| PR | $C_i = C_{in,i}$<br>$T = T_{in}$<br>$u = u_{valve}$ | $\partial C_i / \partial z = 0$<br>$\partial T / \partial z = 0$<br>$u = 0$ |
| AB | $D_z \cdot \partial C_i / \partial z = u_{AB}(C_i - C_{in,i})$<br>$\lambda_{eff} \cdot \partial T / \partial z = \rho_g c_{pg} u_{AB}(T - T_{in})$<br>$u = u_{AB}$ | $\partial C_i / \partial z = 0$<br>$\partial T / \partial z = 0$<br>$P = P_{out}$ |
| DP | $\partial C_i / \partial z = 0$<br>$\partial T / \partial z = 0$<br>$u = 0$ | $\partial C_i / \partial z = 0$<br>$\partial T / \partial z = 0$<br>$u = u_{valve}$ |

| | | |
|---|---|---|
| RE | $D_{z,i} \cdot \partial C_i / \partial z = u_{RE}(C_i - C_{in,i})$<br>$\lambda_{eff} \cdot \partial T / \partial z = \rho_g c_{pg} u_{RE}(T - T_{in})$<br>$u = u_{RE}$ | $\partial C_i / \partial z = 0$<br>$\partial T / \partial z = 0$<br>$P = P_{out}$ |
| DE | $\partial C_i / \partial z = 0$<br>$\partial T / \partial z = 0$<br>$P = P_{out}$ | $D_{z,i} \cdot \partial C_i / \partial z = u_{DE}(C_i - C_{in,i})$<br>$\lambda_{eff} \cdot \partial T / \partial z = \rho_g c_{pg} u_{DE}(T - T_{in})$<br>$u = u_{DE}$ |

The model parameters are listed in Table 2:

Table 2 Experimental parameters used for model validation

| Item | Symbol | Unit | Value |
|---|---|---|---|
| Reactor inner diameter | $D_t$ | m | 0.0206 |
| Bed length (Reactor) | $L_{bed}$ | m | 0.586 |
| Mass of sorbent | $m_{sorbent}$ | g | 357.64 |
| Bulk density of sorbent | $\rho_b$ | kg/m$^3$ | 1830 |
| Apparent density of pellets | $\rho_p$ | kg/m$^3$ | 3380 |
| Bed voidage | $\varepsilon_b$ | - | 0.46 |
| Specific heat capacity of solids | $c_{ps}$ | J/(K·kg) | 650 |
| Equivalent sorbent particle size | $d_p$ | mm | 4 |
| Inlet temperature | $T_{in}$ | °C | 600 |
| Tubular wall temperature | $T_w$ | °C | 600 |
| Absorption pressure | $P_{AB}$ | kPa | ~280 |
| Desorption pressure | $P_{DE}$ | kPa | 110 |
| Absorption time | $t_{AB}$ | s | 26~296 |
| Depressurization time | $t_{DP}$ | s | 5 |
| Recycle time | $t_{RE}$ | s | 0, 5, 6, 7 |
| Desorption time | $t_{DE}$ | s | 30~300 |
| Pressurization time | $t_{PR}$ | s | 4 |

| | | | |
|---|---|---|---|
| Inlet air flow rate | $Q_{air}$ | SLPM | 1, 2, 3 |
| Inlet steam flow rate | $F_{steam}$ | mol/min | 0.1 |
| Valve coefficients at PR/DP steps | $C_v$ | $m \cdot s\sqrt{mol \cdot K}$ | $1.1\times10^{-8}$/$2.3\times10^{-8}$ |

2.6. Solution method and optimization scheme

The 1D model was developed with FORTRAN code. The partial differential equations (PDEs) were converted into algebraic equations using the finite difference method. The bed geometry was discretized in the axial direction into 30 volume elements of the same size. The set of non-linear equations was solved by using the IMSL numerical library (Rogue Wave Software).

The simulation is iterated until it reaches a cyclic steady state (CSS). In the present work, the criterion for CSS was defined as <0.1% relative change in $O_2$ purity and productivity between two consecutive iterations. Four indicators at the CSS are used to evaluate the performance of $O_2$ separation, i.e., $O_2$ purity, $O_2$ productivity, $O_2$ recovery, and power consumption. The dead zone in the downstream packed bed strongly affects the $O_2$ purity in the product. Therefore, it was also considered in the calculation. For simplification, $N_2$ and $O_2$ in the dead zone were added to the $O_2$ product during the desorption process. The gas concentrations in the dead zone were the same as the outlet gas concentrations at the last step (DP or RE step), and the $V_{dead}$ was obtained by fitting the experimental results.

The four performance indicators are defined as:

$$O_2\ purity\ (\%) = \frac{Total\ moles\ of\ O_2\ product\ in\ \text{the}\ desorption\ step}{Total\ moles\ of\ N_2 + O_2\ in\ product\ in\ \text{the}\ desorption\ step} \times 100\% \quad (12)$$

$$O_2\ recovery\ (\%) = \frac{Total\ moles\ of\ O_2\ product\ \text{from the}\ desorption\ step}{Total\ moles\ of\ O_2\ fed\ into\ the\ column\ in\ one\ cycle} \times 100\% \quad (13)$$

$$O_2\ \text{productivity}\ (g_{O_2} \cdot g_{sorbent}^{-1} \cdot h^{-1}) = \frac{Total\ moles\ of\ O_2\ product\ in\ \text{the}\ desorption\ step}{m_{sorbent}\ \times\ one\ cycle\ time} \quad (14)$$

$$\text{Power consumption}\ (\text{kW} \cdot \text{h/ton}\ O_2) = \frac{E_{PR} + E_{AB} + E_{DE}}{Mass\ of\ O_2\ product\ in\ desorption\ step} \quad (15)$$

The power consumption in this study is reported in terms of the electricity equivalent to produce 1 ton $O_2$, i.e., kW·h/(ton $O_2$). $E_{PR}$ and $E_{AB}$ are the power consumption to compress the air from the ambient pressure to the absorption pressure in the pressurization step and the absorption step, respectively. $E_{DE}$ is the power consumption used to generate steam in the oxygen desorption step.

As the absorption pressure was not very high, multi-stage compression with inter-cooling is not necessary. The adiabatic compression process was used to estimate the power consumption for air compression, which is described by Eq.(16). The compression coefficient $\eta_c$ was assumed to be 0.85.

$$E_{PR} + E_{AB} = \int_0^{t_{PR}+t_{AB}} \frac{\dot{n}_{feed} RT}{\eta_c} \frac{\gamma}{\gamma - 1} \left[ \left( \frac{P_{in}}{P^0} \right)^{\frac{\gamma-1}{\gamma}} - 1 \right] dt \quad (16)$$

The energy penalty of the steam generation was fully considered in the current study. Based on the process of integrating the steam production with the heat recovery in our previous work [71], the production of 1 kg of 600 °C steam consumes 121 kJ (electricity equivalent) when heat integration is considered. Thus, the power consumption related to steam generation in each cycle can be determined by the desorption time and the steam flow rate. A more

conservative steam energy consumption of 121 kJ/kg was used in the current study when compared to our previous study (80 kJ/kg). The detailed energy consumption for each unit is listed in Table S1. Based on our previous process simulation study [71], other energy consumptions such as heat loss from the reactor wall and supplemental preheating requirement for air beyond heat exchange with the exhaust gas are very small when compared to steam-related energy consumption.

The model fitting and experimental validation were carried out as the following steps: (1) Fit the $k_{AB}$ based on the breakthrough curve; (2) Fit $C_v$ for both PR and DP steps based on the experimental pressure curves. (3) Fit $k_{DE}$ based on the experimental measurement of $O_2$ productivity obtained with parts of experimental data; (4) Verify $k_{DE}$ with all experimental data of $O_2$ productivity; (5) Fit $V_{dead}$ based on the experimental measurement of $O_2$ purity parts of experimental data; (6) Verify $V_{empty}$ with all experimental data of $O_2$ purity.

The $O_2$ purity, $O_2$ productivity, and power consumption are all critical in the practical application, but it is difficult to achieve the optimal condition of these parameters at the same time. The multi-objective optimization was conducted to obtain a tradeoff relationship between these parameters. Seven decision variables were considered, i.e., absorption pressure, bed length, absorption time, desorption time, air flow rate, steam flow rate, recycle time. The optimization framework was modified from a non-dominated sorting genetic algorithm with jumping gene adaptation (NSGA-II-aJG) developed by Gupta et al. [72, 73]. The decision variables created by the NSGA-II-aJG operator were used as the input of the 1D model, and the performance indicators obtained by the 1D model were further used as the fitness

functions for determining the Pareto fronts. The population size and the generation size in the genetic algorithm were set to be 50 and 70, respectively, in the current work. The optimization conditions are listed in Table 3:

Table 3. Optimization conditions

| Item | Unit | Case1 | Case2 | Case3 | Case4 | Case5 | Case6 | Case7 |
|---|---|---|---|---|---|---|---|---|
| $t_{AB}$ | s | 30~270 | | | | | | |
| $t_{DP}$ | s | 30~270 | | | | | | |
| $L_{bed}$ | m | 0.29~1.16 | | | | | | |
| $F_{steam}$ | mol/s | 0.05~0.20 | | | | | | |
| $P_{AD}$ | kPa | 120~300 | | | | | | |
| $Q_{air}$ | SLM | 0.5~5 | | | | | | |
| $t_{RE}$ | s | 0 | | 1~8 | 0 | | 1~8 | |
| $V_{dead}$ | L | 0.058 | | 0.058 | 0.058 | 0.012 | 0.058 | 0.012 |
| $O_2$ purity | % | >90 | >95 | >95 | - | | | |
| Optimization objective | - | Max: $O_2$ productivity<br>Min: Power consumption | | | Max: $O_2$ purity<br>Min: Power consumption | | | |

## 3. Results and Discussion

### 3.1. Experimental verification

As shown in Fig.3, SCFC8291 spontaneously released $O_2$ even at relatively high $O_2$ partial pressures. The oxygen non-stoichiometry changed from around 0.309 to 0.473, by switching gas from 50% $O_2$ to 0.2% $O_2$ at 600 $^oC$, corresponding to around 1.5 wt% of oxygen capacity.

In order to accurately quantify the equilibrium limitations for oxygen release and uptake, which is important for the LDF based kinetic model, a 9-parameter empirical equation was fitted to predict the non-stoichiometry at different pressures and temperatures. The maximum relative deviation between the prediction and experiment was less than 2%, which was sufficiently accurate to describe the non-stoichiometry.

$$\begin{aligned}\log_{10}\left(\frac{\delta}{0.5-\delta}\right) = & -9.378 - 0.6406\times\log_{10}(\mathrm{P_{O_2}}/\mathrm{P^0}) - 0.1744\times\left[\log_{10}(\mathrm{P_{O_2}}/\mathrm{P^0})\right]^2 \\ & - 0.2105\times\left[\log_{10}(\mathrm{P_{O_2}}/\mathrm{P^0})\right]^3 + 1.2424\times10^{-3}\times T \\ & + 1.1578\times10^{-3}\times\log_{10}(\mathrm{P_{O_2}}/\mathrm{P^0})\cdot T - 4.4444\times10^{-4}\times\left[\log_{10}(\mathrm{P_{O_2}}/\mathrm{P^0})\right]^2\cdot T \\ & - 8.3776\times10^{-7}\times\log_{10}(\mathrm{P_{O_2}}/\mathrm{P^0})\cdot T^2 - 3.5545\times10^{-4}\times\left[\log_{10}(\mathrm{P_{O_2}}/\mathrm{P^0})\right]^2\cdot T^2\end{aligned} \quad (17)$$

The effects of $k_{AB}$ on the absorption breakthrough curves are shown in Fig. 3. The $O_2$ absorption rate increased with $k_{AB}$ in the LDF model, which leads to a shorter time to reach the equilibrium. The breakthrough of the packed bed only occurs when all the sorbents are contacted with $O_2$. When the $k_{AB}$ is close to 0, the $O_2$ absorption rate is very slow. Therefore, only a small amount of $O_2$ is removed from the air stream. The whole packed bed would be immediately penetrated by the $O_2$ reaction front. On the other hand, an infinitely large $k_{AB}$ would consume the $O_2$ instantly and achieve a vertical breakthrough curve. In other words, a steeper breakthrough curve can be obtained by a larger $k_{AB}$. The breakthrough curve predicted with the $k_{AB}$ of 0.033 matched the experimental data well and was used in the following simulations. As shown in Fig.3c, the modeling results accurately captured the stage of temperature increasing caused by the fast oxygen absorption. The maximum increment of the predicted temperature was about 14 $^{o}$C, which was very close to the experimental value. We

also note that the predicted temperatures decreased more rapidly than the experimental results after the reaction front passed the measurement position of the thermocouple. One possible reason may be the feedback control of the tube furnace. For the period of 700 s – 1200 s, the furnace temperature was increased, by the PID control, to compensate for the impact of the fast decrease in the bed temperature. In contrast, our model assumed a fixed wall temperature of 873 K. The additional heat from the furnace would slow down the decrease of the bed temperature in the experiments. In addition, when the $O_2$ concentration was close to the equilibrium (i.e., 20.9%), the reaction rate became much slower. The intrinsic reaction kinetics replaced the dominant role of the mass transfer. In that case, the apparent reaction rate described by the linear driving force model might predict a faster ending of absorption reaction, while the experiment had a longer delay. Since the temperature deviation was very small (<8 $^{o}$C throughout the experiment), the current model is adequate to predict the experimental results.

.

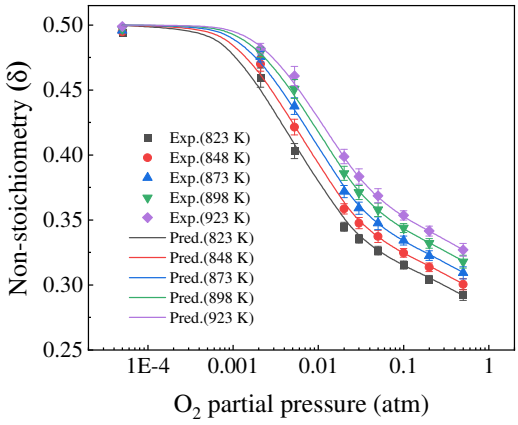


(a)

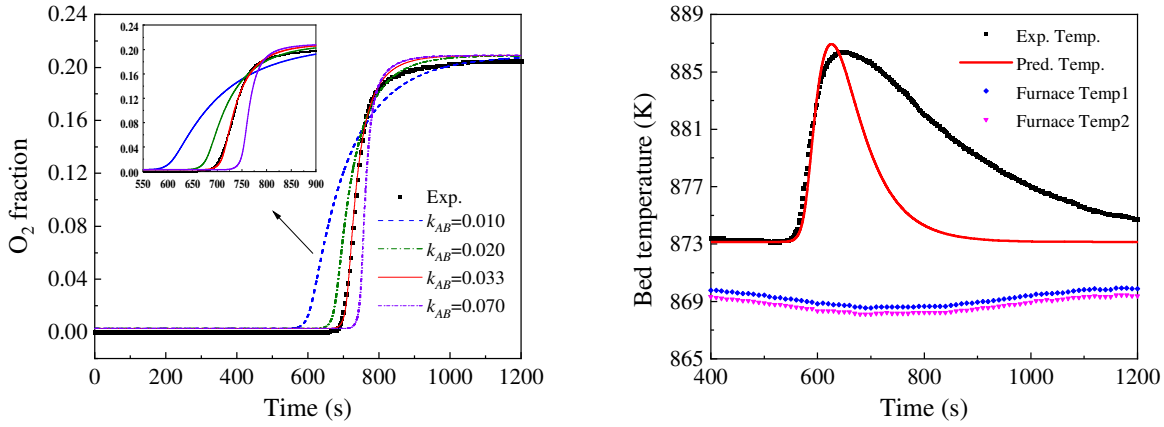


(b) (c)

Fig. 3 (a) Oxygen non-stoichiometry at different temperatures and $O_2$ partial pressures; (b) Effects of $k_{AB}$ on the modeling results of absorption breakthrough curves ($T_{in}$=600 °C, $Q_{air}$=1 SLM, $P_{AB}$=246 kPa); (c) Modeling results of bed temperature with the best-fit $k_{AB}$ =0.033 ($T_{in}$=600 °C, $Q_{air}$=1 SLM, $P_{AB}$=246 kPa) and experimental results of bed temperature and furnace temperatures (based on the thermocouples embedded in the furnace refractory).

Similar to $k_{AB}$, a larger $k_{DE}$ leads to a faster desorption rate and a higher $O_2$ production each cycle. As shown in Fig. S4, $k_{DE}$=0.118 gave the smallest standard deviation from the experimental data. As shown in Fig. 4a and Fig. S5, the model slightly underpredicted the experimental data for most cases, but the deviations were within the acceptable range. The maximum error was 23.5%, and 82% of data fell within ±15% deviation. Apart from the reason discussed above, another potential reason for this underprediction is the nonideal performance of the back-pressure regulator (BPR). As shown in Fig. S3, during the pressurization step, the measured pressure gradually increased to the desired value. This indicates that the BPR does not completely shut off when the pressure is lower than the setting value. Therefore, the actual air flow can be slightly higher than the nominal air flow

during this period, leading to higher oxygen uptake by the sorbent and hence larger oxygen release in the subsequent desorption step. We note that a slight underprediction by the model would be acceptable since the model would provide a conservative projection of the CLAS performance. The above validation of the experimental results also confirms that the LDF models are able to predict the $O_2$ absorption and desorption rates in the packed bed with reasonable accuracy.

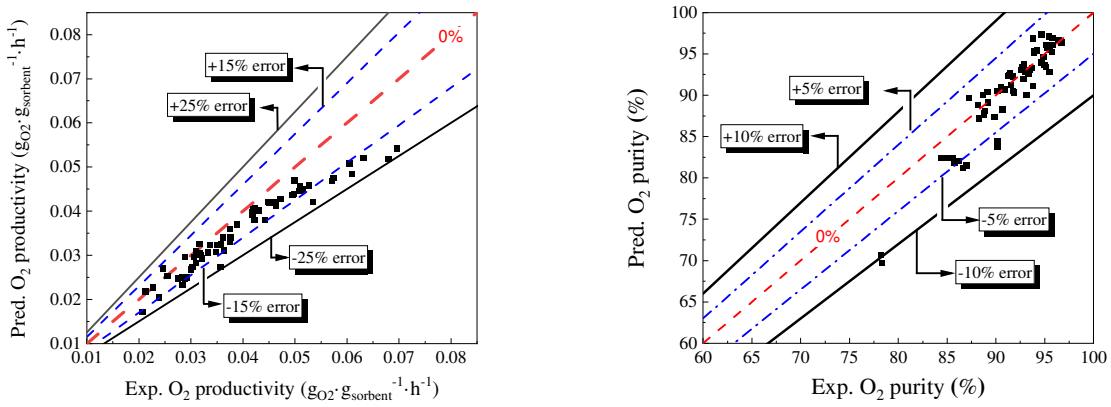


(a) (b)

Fig. 4 Comparison of relative deviations between experimental measurement and modeling prediction for the 4-step cycle configuration (a) $O_2$ productivity and (b) $O_2$ purity.

The residual $N_2$ in the empty volume downstream of the packed bed will negatively affect the $O_2$ purity in the product. Since it is difficult to accurately measure the empty volume due to the complex geometry of the downstream assemblies, experimental data were used to fit the volume (Fig. S6). The smallest standard deviation was achieved at $V_{dead}$=0.058 L. Smaller $V_{dead}$ values would overestimate the $O_2$ purity and vice versa. As shown in Fig. 4b, 90% of predictions fell within ±5% deviation, and 82% were within ±3% deviation. The detailed experimental and modeling results are shown in Fig. S7. Two points with 10% error

correspond to experiments carried out at $t_{AB}$=30 s and $Q_{air}$=1 SLM. The frequent gas switching and the low air flow rate are likely to be the reasons for the larger discrepancies under this condition.

### 3.2. Parametric analysis

The effects of desorption time on $O_2$ purity, recovery, and productivity, and power consumption are shown in Fig. 5. The $O_2$ release increased with the increase in the desorption time. As such, the $O_2$ purity and recovery increased with the desorption time. However, there existed extremums for $O_2$ productivity and power consumption. The difference of non-stoichiometry, which is the driving force of the $O_2$ release based on Eq.(10), will decrease with the increase in the desorption time, and the $O_2$ release rate also follows the same trend. The $O_2$ productivity initially increased with the desorption time due to the larger $O_2$ recovery. However, as the $O_2$ release rate is inversely proportional to the cycle time, the rate decrease eventually led to a decrease in the $O_2$ productivity. The power consumption shows an opposite trend. An increase in the desorption time increased both the steam-related power consumption and the $O_2$ production. The faster growth in the $O_2$ production significantly reduced the power consumption at the initial stage, reaching a minimum at around 125 s desorption time. This is followed by a gradual increase in power consumption as the increase in oxygen production slows down relative to the increase in steam consumption.

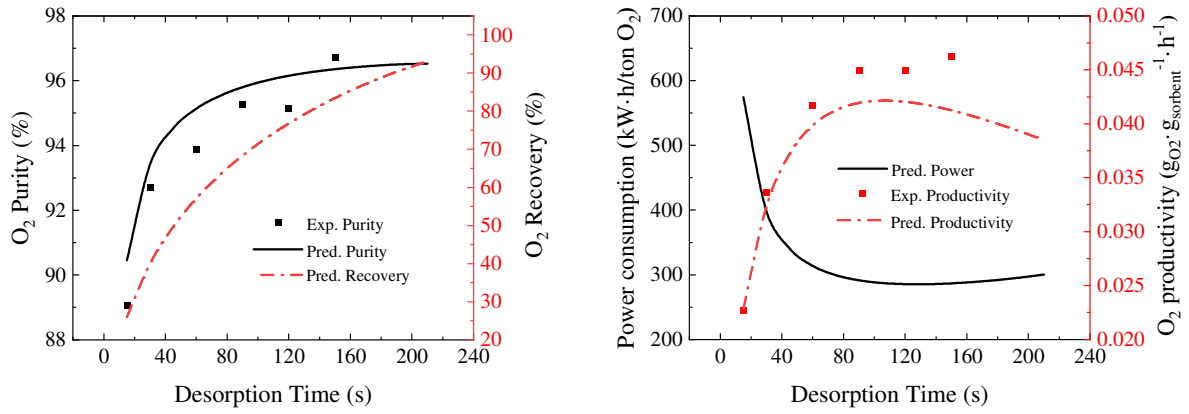


(a) (b)

Fig. 5 Effects of desorption time on (a) $O_2$ purity and recovery, and (b) $O_2$ productivity and power consumption ($t_{AB}$=150 s, $Q_{air}$=2 SLM).

The effects of absorption time on the four performance indicators are shown in Fig. 6 a and b. The $O_2$ absorption amount increased with the absorption time. As a result, the $O_2$ release also increased, leading to a higher $O_2$ purity. The $O_2$ volume fraction profiles along the bed are shown in Fig. 7. At first, the increase in the absorption time increased the $O_2$ concentration in the packed bed, and the increased $O_2$ storage in the sorbents would be released in the desorption step (Fig. 6a). The rapid increase in $O_2$ productivity, up to around 75 seconds for the absorption step, leads to a decrease in power consumption (Fig. 6b). Meanwhile, increased absorption time leads to $O_2$ breakthrough, thereby lowering $O_2$ recovery.

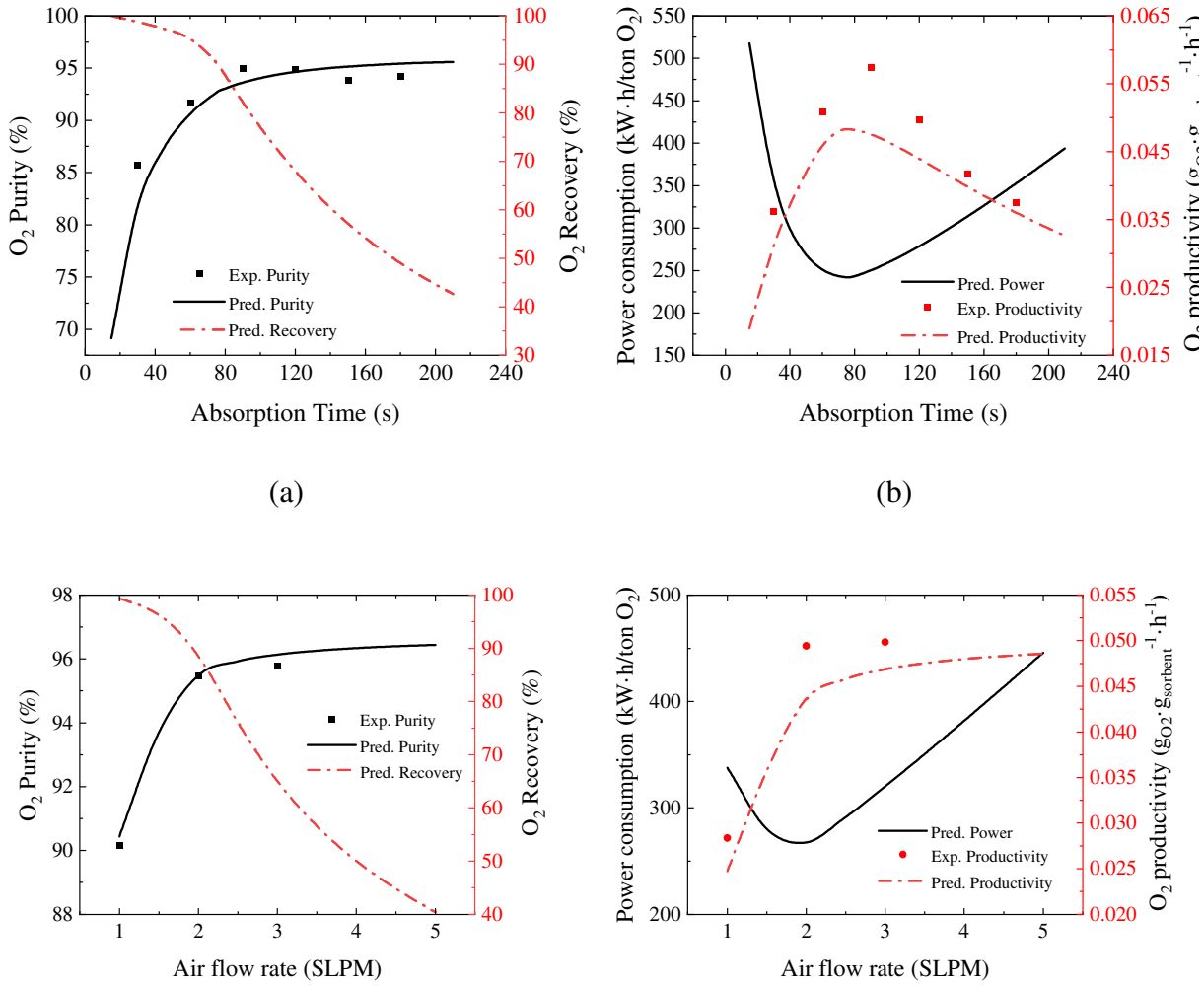


Fig. 6 (a-b) Effects of absorption time on (a) $O_2$ purity and recovery, and (b) $O_2$ productivity and power consumption ($t_{DE}$=60 s, $Q_{air}$=2 SLM). (c-d) effects of air flow rate on (c) $O_2$ purity and recovery, and (d) $O_2$ productivity and power consumption ($t_{AB}$=120 s, $t_{DE}$=120 s)

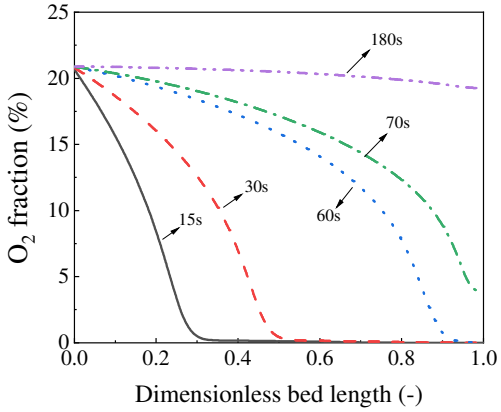


Fig. 7 Axial profiles of the $O_2$ volume fraction at the end of the absorption step when the simulation reached CSS with different absorption time

With the desorption time fixed at 60 seconds, a further increase in the absorption time above 75 seconds would not lead to additional benefits since the absorbed oxygen cannot be fully recovered by the steam purge. As such, $O_2$ would gradually accumulate in the packed bed with the cyclic operation, and the $O_2$ reaction front at the end of the absorption step would finally penetrate the entire bed at the cyclic steady state (CSS) condition. As a result, the $O_2$ recovery rapidly decreases with the increased absorption time. In addition, both the compression work and the overall cycle time would increase with increasing absorption time. These factors lead to decreased $O_2$ productivity and increased power consumption when the absorption time exceeds 75 seconds. The varying trends of $O_2$ productivity and power consumption indicate that there exists a best match between the $O_2$ absorption time/amount and the $O_2$ desorption time/amount, which can maximize $O_2$ productivity and minimize power consumption.

The effects of air flow rate were similar to those of the absorption time. As shown in Fig. 6 c and d, higher $O_2$ purity and lower $O_2$ recovery were obtained at a larger air flow rate. The

power consumption reached a minimum value and then increased. The only difference was that the $O_2$ productivity continuously increased with the air flow rate. This is because of the fixed cycle time and the increasing amount of $O_2$ release. It should be noted that if the absorption time is sufficiently long, the breakthrough curve in the packed bed can be formed even at a low air flow rate. In other words, the minimum power consumption will shift towards the lower air flow rate with increasing absorption time.

As shown in Fig. 8 a and b, $O_2$ purity, recovery, and productivity, and power consumption increased with the absorption pressure. The difference in oxygen non-stoichiometry values in the absorption and desorption steps increases with the absorption pressure. As such, more $O_2$ can be released at a higher absorption pressure. The $O_2$ purity, recovery, and productivity accordingly increased with the absorption pressure. However, the compression work increased faster than the $O_2$ productivity. As a result, the power consumption also increased with the absorption pressure. Fig.8 c and d summarizes the effect of steam flow rate in the desorption step. An increase in the steam flow rate leads to a larger driving force for $O_2$ desorption. This leads to higher $O_2$ purity, recovery, and productivity. Meanwhile, power consumption related to steam generation linearly increases with the steam flow rate, which is at a faster pace than the increase in $O_2$ production. Compression work initially dominates the overall power consumption. Therefore, the power consumption decreases with increasing steam flow at low steam flow rates (<0.12 mol/s). A further increase in steam flow rate would lead to an increase in power consumption since the steam-related energy consumption more than offsets the increase in oxygen productivity.

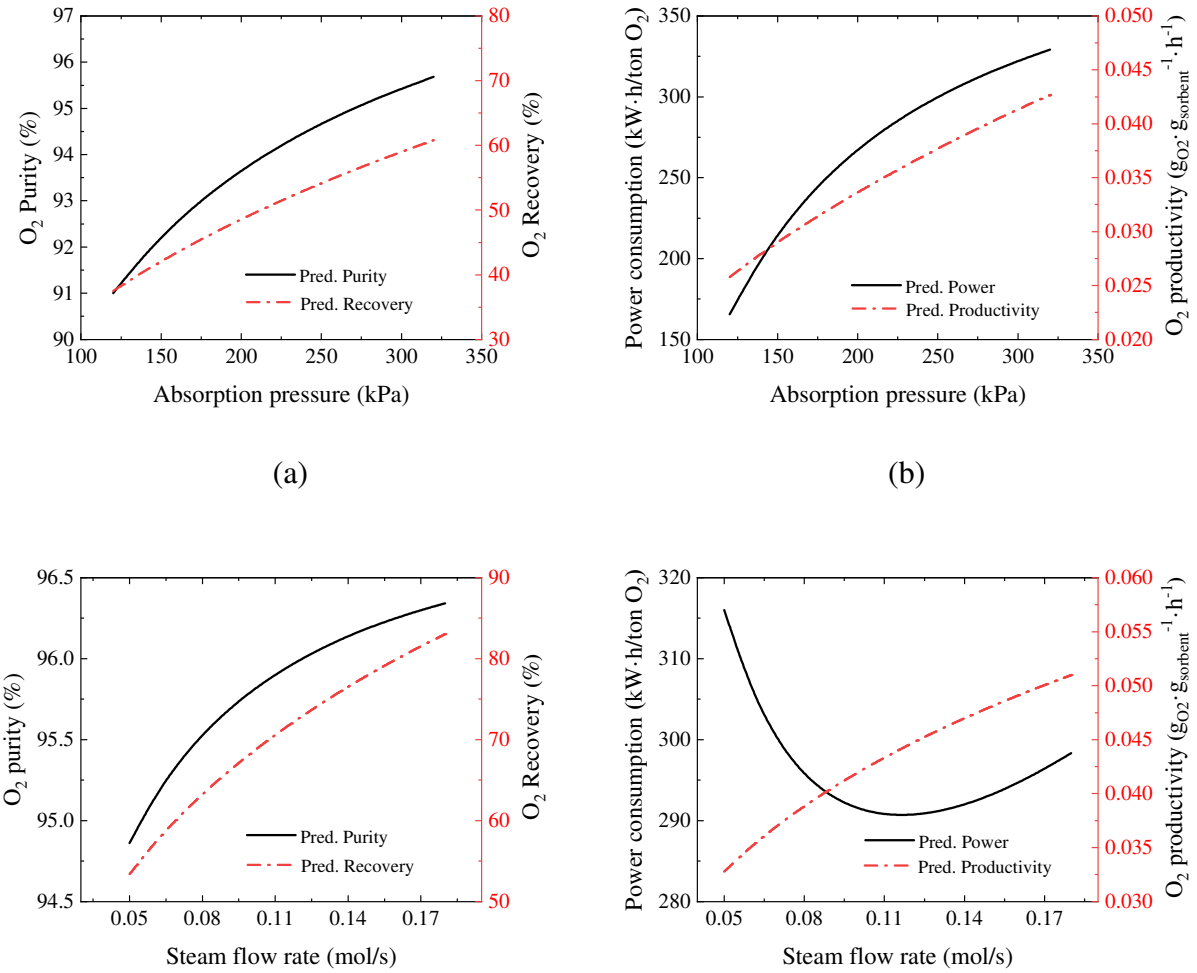


Fig. 8 (a-b) effects of absorption pressure on $O_2$ purity and recovery, and (b) $O_2$ productivity and power consumption ($t_{AB}$=150 s, $t_{DE}$=60 s, $Q_{air}$=2 SLM). (c-d) effects of steam flow rate on (a) $O_2$ purity and recovery, and (b) $O_2$ productivity, and power consumption ($t_{AB}$=150 s, $t_{DE}$=90 s, $Q_{air}$=2 SLM)

The gas impurity (i.e., $N_2$) in the bed void and the dead volume will reduce the $O_2$ purity and hence the product quality. To improve oxygen purity, the effect of an oxygen recycle step was investigated. Since the purity of the $O_2$ product was >90% under most experimental conditions, most impurities in the column would have already been removed under typical operating conditions. As shown in Fig. 9, with an increase in the recycle time, the gas

impurity was gradually purged from the system, so the $O_2$ purity increased accordingly. As part of the $O_2$-enriched stream was consumed in the recycle step, the $O_2$ recovery decreased with the recycle time. The nominal $O_2$ productivity was calculated by using the data log of the $O_2$ analyzer at the outlet of the packed bed. The recycle step provided additional $O_2$ to the sorbents, so the nominal $O_2$ productivity increased with the recycle time. However, the real $O_2$ productivity decreased because of the consumption of $O_2$ in the recycle step and a longer total cycle time. The comparisons of $O_2$ productivity and $O_2$ purity between experimental measurement and modeling prediction for the 5-step cycle configuration are shown in Fig. S8. The average deviation of the $O_2$ purity was 1.6%, and the average deviation of the $O_2$ productivity was 9.1%. The prediction matched well with the variation in the experimental results. Therefore, the current model is deemed to be applicable for predicting the 5-step cycle structure.

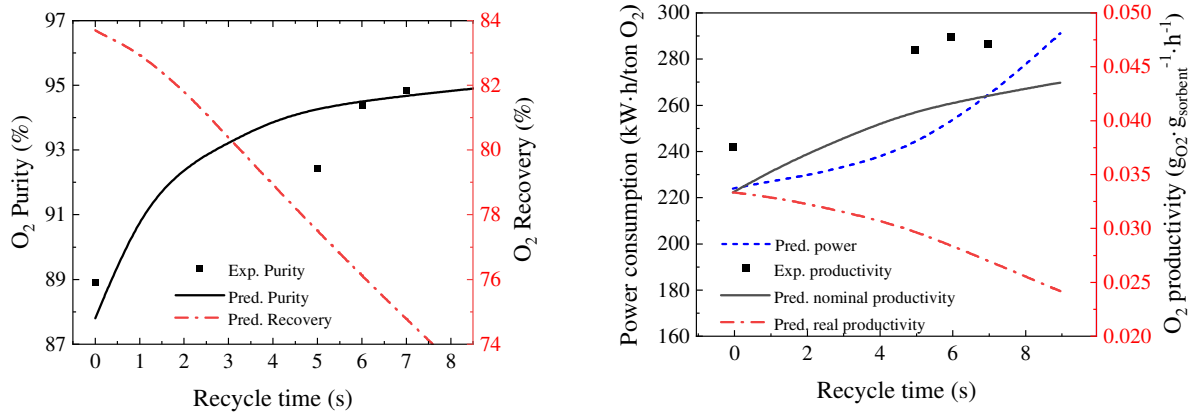


(a) (b)

Fig. 9 (a-b) Effects of recycle time on (a) $O_2$ purity and recovery, and (b) $O_2$ productivity and power consumption ($t_{AB}$=90 s, $t_{DE}$=30 s, $Q_{air}$=1 SLM)

Table 4 summarizes the impacts of operating parameters on the performance indicators. As can be seen, $O_2$ purity and recovery monotonically change with the absorption time, desorption time, air flow rate, steam flow rate, and absorption pressure. In comparison, $O_2$ productivity and power consumption can be maximized and minimized, respectively, by specific combinations of different operational parameters. These optimal conditions are further presented as the Pareto fronts in the next section.

Table 4. The impacts of operating parameters on the performance indicators ("+": positive impact; "-": negative impact; "+/-": maximum value existing; "+/-": minimum value existing)

| | $t_{AB}$ | $t_{DE}$ | $t_{RE}$ | $P_{AB}$ | $F_{steam}$ | $Q_{air}$ |
|---|---|---|---|---|---|---|
| $O_2$ purity | + | + | + | + | + | + |
| $O_2$ recovery | - | + | - | + | + | - |
| $O_2$ productivity | +/- | +/- | - | + | + | + |
| Power consumption | -/+ | -/+ | - | + | -/+ | -/+ |

3.3. Process optimization

The calculated Pareto fronts for maximizing the $O_2$ productivity and minimizing the power consumption are shown in Fig. 10a. All the points at the Pareto fronts meet the specific requirements of $O_2$ purity, and each point represents the minimum power consumption for obtaining a specific $O_2$ productivity. The power consumption increased with the $O_2$ productivity. For the 4-step cycle configuration, the maximum productivity for producing ≥ 90% purity $O_2$ was 0.10 $g_{O2}/(g_{sorbent}\cdot h)$ with 381 kW·h/(ton $O_2$). Fig. 10b shows the energy distribution between steam generation and compression work of three specific conditions, the

corresponding operational parameters are listed in Table S2. Steam generation accounts for a majority of the power consumption at low $O_2$ productivity levels. The proportion of compression work in the total power consumption increases with the $O_2$ productivity, so is the total power consumption. This is because a higher absorption pressure was preferable for the higher $O_2$ productivity, but the total power consumption would also increase with the absorption pressure. The power consumption was significantly increased when the requirement of $O_2$ purity rose from 90% to 95%. A higher $O_2$ purity required larger air and steam flow rates and longer absorption time, leading to higher energy consumption.

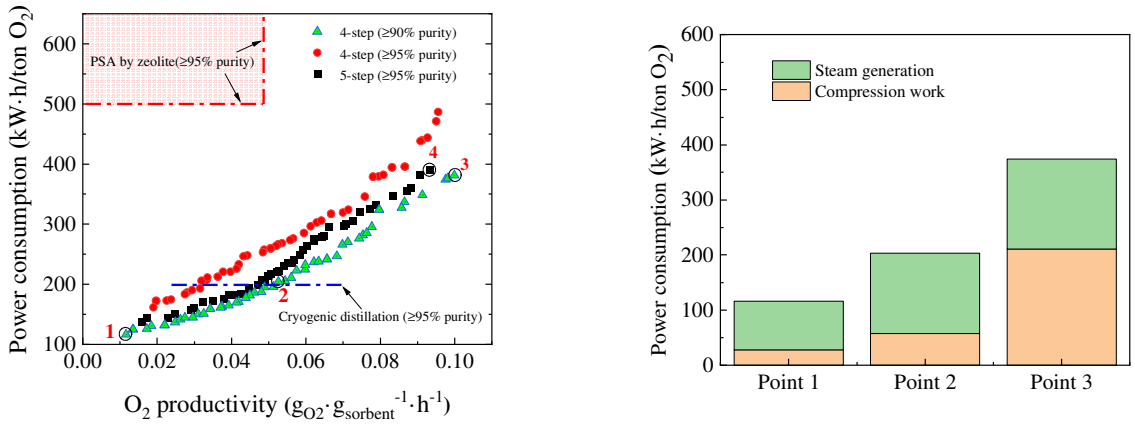


(a) (b)

Fig. 10 (a) Power consumption-productivity Pareto fronts for the 4-step and 5-step cycle configurations that meet the specific requirements of $O_2$ purity, the red dash lines show the $O_2$ productivity and power consumption to produce ⩾95% purity $O_2$ using the conventional PSA [12, 14], the blue dash line shows the power consumption to produce ⩾95% purity $O_2$ using cryogenic distillation [6]; (b) Breakdown of the energy consumptions for specific conditions at the Pareto front.

To further investigate the effects of $O_2$ purity on power consumption, the Power consumption-purity Pareto fronts were calculated. They are illustrated in the vertical plane in Fig. 11. Each point at the Pareto front represents the minimum power consumption for achieving a specific $O_2$ purity. The corresponding $O_2$ productivities for these points are shown in the horizontal plane. More power is consumed to produce higher purity of $O_2$. For the 4-step cycle configuration with $V_{dead}$=0.058 L, the minimum power consumption for producing 1 ton $O_2$ with ≥90% purity is 115 kW·h, and this increases to 161 kW·h for producing 1 ton $O_2$ with ≥95% purity. The $O_2$ purity is limited to 98.2% due to the existence of the dead volume. When the requirement of the $O_2$ purity is close to the constraint boundary, increasing absorption pressure would be necessary to further improve the $O_2$ purity. However, this pressurization process is highly energy-consuming.

Another approach to improve the $O_2$ purity is to purge the packed bed with the $O_2$ product. Thus, the power consumption-productivity Pareto front for the 5-step cycle configuration was also calculated. Even though the recycle step would consume a small amount of $O_2$, it is an effective approach to increase the $O_2$ purity. As shown in Fig. 10a, the power consumption for producing $O_2$ with 95% purity shifted down by more than 30 kW·h/(ton $O_2$), and the maximum $O_2$ productivity reached 0.0932 $g_{O2}/(g_{sorbent}\cdot h)$ with 390 kW·h/(ton $O_2$). It is therefore more efficient to adopt the 5-step configuration to produce higher purity $O_2$.

As can be seen, CLAS is highly competitive in terms of all the major performance indicators when compared with conventional PSA. The minimum power consumption for producing 1 ton $O_2$ with the 95% purity is above 500 kW·h for the conventional PSA

technology [14, 74], while the minimum power consumption is reduced to 161 kW·h for the simple 4-step CLAS cycle configuration and further reduced to 118 kW·h/(ton $O_2$) for the 5-step CLAS cycle configuration. The reported $O_2$ productivity in the literature for the conventional PSA to produce ~95% purity $O_2$ was typically below 0.048 $g_{O2}/(g_{sorbent}\cdot h)$ with a substantially higher power consumption of >500 kW·h/(ton $O_2$). In contrast, $O_2$ productivity can be doubled using the 5-step CLAS to produce ⩾95% purity $O_2$ with a much lower power consumption. It should be noted that the aforementioned power consumption and $O_2$ productivity are based on the commercial tonnage scale $O_2$ production. The $O_2$ productivity of a conventional PSA system can be enhanced by a short cycle time and a small length-to-diameter in some small-scale conditions, such as the medical oxygen concentrator [76]. However, for commercial tonnage scale $O_2$ plants, the fast gas switching (<10s cycle time) is difficult to guarantee the gas uniformity and eliminate the negative impact of stagnant zone on the $O_2$ purity.

Compared to cryogenic ASU which has a typical power consumption of 200 kW·h/ton $O_2$ (at 95% purity) [6], CLAS with the SCFC sorbent is also highly attractive. We note that the current CLAS configuration is not very efficient in producing ultra-high-purity (≥99%) $O_2$, mainly due to the dead volume downstream of the bed in the current reactor setup. If the dead volume is minimized, the CLAS performance would be significantly better. The power consumption-purity Pareto fronts were calculated for a PSA system with 20% of the current dead volume. For the 4-step cycle configuration, the minimum power consumption for realizing the 95% $O_2$ purity dropped from 161 kW·h/(ton $O_2$) to 137 kW·h/(ton $O_2$). The maximum $O_2$ purity also increased from 98.3% to 99.0%. For the 5-step cycle configuration,

the maximum theoretical $O_2$ purity could be raised up to almost 99.9%. The minimum power consumption for producing 1 ton $O_2$ with 99% purity was reduced from 280 kW·h to 130 kW·h, much lower than ~300 kW·h//(ton $O_2$) for the conventional cryogenic distilling method and ~870 kW·h//(ton $O_2$) for the conventional PSA method with at a comparable 99% purity [7,8,76]. The above calculation indicates that with the minimized dead volume and the suitable cycle configuration, CLAS can be significantly more efficient than cryogenic distillation even when the $O_2$ purity is required up to 99%. We also note that the above calculation converts the heat consumed for steam generation into an electricity-equivalent form, using a conservative energy conversion coefficient. As such, CLAS can be even more advantageous when integrated with a thermochemical process, e.g., IGCC or oxyfuel combustion, from an energy efficiency standpoint. Although CLAS is quite promising from an energy efficiency standpoint, a comprehensive economic assessment is desirable for future studies to confirm its economic benefits.

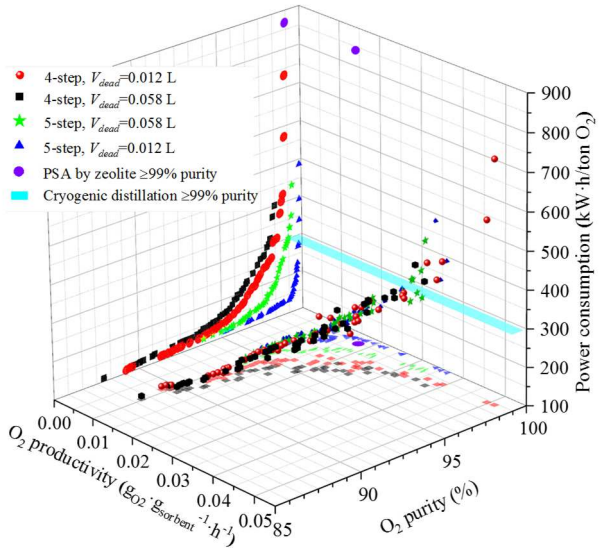


Fig. 11 Power consumption-purity Pareto fronts for the different cycle configurations and

different dead volumes with corresponding $O_2$ productivities illustrated in the horizontal plane.

## 4. Conclusion

In this work, a 1D packed bed model for chemical looping air separation (CLAS) was developed and experimentally validated under a wide range of operating parameters using a SCFC8291 perovskite sorbent. The experimentally validated model was then used to evaluate and optimize the performance of the CLAS process. Our studies indicated that linear driving force (LDF) models can accurately predict absorption and desorption kinetics after incorporating the $O_2$ non-stoichiometry data of the sorbent. Simulation of the packed bed absorber and desorber indicates that $O_2$ purity and recovery monotonically change with the absorption time, desorption time, air flow rate, steam flow rate, and absorption pressure. Meanwhile, extremums for $O_2$ productivity and power consumption were achieved by a tradeoff between the $O_2$ absorption amount and the $O_2$ desorption amount. For a 4-step cycle configuration, the minimum power consumption for producing 1 ton $O_2$ with ≥90% purity is 115 kW·h and the value increases to 161 kW·h/(ton $O_2$) if 95% purity is required. The required $O_2$ purity has a major impact on power consumption. Adding an oxygen product recycle step in the pressure swing absorption (PSA) operation can substantially improve the $O_2$ purity without decreasing the $O_2$ productivity by a significant extent. As a result, the 5-step cycle configuration notably reduced the minimum power consumption from 161 to 118 kW·h/(ton $O_2$)at 95% purity. The maximum $O_2$ productivity reached 0.0932 $g_{O2}/(g_{sorbent}\cdot h)$ at 390 kW·h/ton $O_2$ (95% pure). The optimization results indicate that CLAS can be highly competitive compared to the conventional PSA or cryogenic distillation. Minimizing the

downstream dead volume of the CLAS based PSA system can further increase the process efficiency, allowing the production of 99% pure oxygen with <50% energy consumption when compared to cryogentic distillation. Although the current study focused exclusively on optimizing the process performance with a single, high-performance sorbent, the model developed can be used to guide sorbent optimization efforts in the future by quantifying desirable sorbent properties and their impacts on CLAS performance.

**Acknowledgment**

This work was supported by the U.S. Department of Energy (Award No. FE0031521), the National Science Foundation (Grant No. CBET-1923468), and the North Carolina State University Kenan Institute for Engineering, Technology, and Science. We acknowledge the use of the Analytical Instrumentation Facility (AIF) at North Carolina State University, which is supported by the State of North Carolina and the National Science Foundation.

**Appendix A. Supplementary data**

Supplementary material related to this article can be found online.

**Appendix B. Nomenclature**

| | |
|---|---|
| $C_i$ | Concentration of gas $i$, mol/m$^3$ |
| $C_v$ | Valve coefficient, $\mathrm{m} \cdot \mathrm{s}\sqrt{mol \cdot K}$ |
| $c_{pg}$ | Specific heat capacity of gas, J/(kg·K) |
| $c_{ps}$ | Specific heat capacity of solids, J/(kg·K) |
| $D_{m,i}$ | Molecular diffusion coefficient of gas $i$, m$^2$/s |
| $D_t$ | Tube inner diameter, m |

| | |
|---|---|
| $D_{z,i}$ | Axial mass dispersion coefficients of gas *i*, $m^2/s$ |
| $d_p$ | Equivalent particle size, m |
| $E_{AB}$ | Power consumed at the absorption step, kW·h |
| $E_{DE}$ | Power consumed at the desorption step, kW·h |
| $E_{PR}$ | Power consumed at the pressurization step, kW·h |
| $F_{steam}$ | Inlet steam flow rate, mol/min |
| $\Delta H_{ab,O_2}$ | Absorption reaction enthalpy of $O_2$, kJ/mol $O_2$ |
| $h_{bed}$ | Heat transfer coefficient of the packed bed, $W/(m^2 \cdot K)$ |
| $h_w$ | Wall heat transfer coefficient, $W/(m^2 \cdot K)$ |
| $k_{LDF}$ | Lumped coefficient of LDF model, dimensionless |
| $k_{AB}$ | Lumped coefficient of LDF model in absorption step, dimensionless |
| $k_{DE}$ | Lumped coefficient of LDF model in desorption step, dimensionless |
| $L_{bed}$ | Bed length, m |
| $MW_g$ | Molar mass of gas mixture, g/mol |
| $MW_O$ | Molar mass of oxygen atom, 16.00 g/mol |
| $MW_{reduced}$ | Molar mass of the fully reduced sample, 150.26 g/mol |
| $MW_s$ | Molar mass of the fresh sample, 179.93 g/mol |
| $m_{reduced}$ | Mass of fully reduced sample, g |
| $m_s$ | Sample mass at a specific state, g |
| $m_{sorbent}$ | Fresh sample mass, g |
| $n_{feed}$ | Molar flow rate of feeding air, mol/s |
| $P_{AB}$ | Absorption pressure, kPa |
| $P_{\mathrm{DE}}$ | Desorption pressure, kPa |
| $P_{high}$ | High pressure, Pa |
| $P_{in}$ | Total pressure at the inlet of the packed bed, atm |
| $P_{low}$ | Low pressure, Pa |
| $P_{O_2}$ | $O_2$ partial pressure, Pa or atm |
| $P^0$ | Standard pressure, 1 atm |
| $Pr$ | Prandtl number, dimensionless |
| $P_t$ | Total pressure, Pa or atm |
| $Q_{air}$ | Inlet air flow rate, SLPM |
| $q_i$ | Absorption amount of gas *i* based on per unit of sorbent, mol/kg |

| | |
|---|---|
| $q^*_{O_2}$ | The amount of $O_2$ absorbed at the equilibrium state, mol/kg |
| $R$ | Ideal gas constant, 8.314 J/(mol·K) |
| $Re_p$ | Reynolds number of particle, dimensionless |
| $\Delta S_{ab,O_2}$ | Absorption reaction entropy, J/(mol·K) |
| $T$ | Temperature, $^o$C or K |
| $T_{\text{in}}$ | Inlet gas temperature, $^o$C or K |
| $T_w$ | Tubular wall temperature, $^o$C or K |
| $t$ | Time, s |
| $t_{AB}$ | Absorption time, s |
| $t_{DE}$ | Desorption time, s |
| $t_{DP}$ | Depressurization time, s |
| $t_{PR}$ | Pressurization time, s |
| $t_{RE}$ | Recycle time, s |
| $U$ | Overall heat transfer coefficient, W/(m$^2$·K) |
| $u$ | Superficial gas velocity based on the empty bed, m/s |
| $u_{AB}$ | Inlet gas velocity at absorption step, m/s |
| $u_{DE}$ | Inlet gas velocity at desorption step, m/s |
| $u_{RE}$ | Inlet gas velocity at recycle step, m/s |
| $u_{valve}$ | Inlet or outlet gas velocity calculated by the valve equation, m/s |
| $V_{dead}$ | Volume of dead zone, L |
| $z$ | Axial position, m |

*Greek letters*

| | |
|---|---|
| $\gamma$ | Ratio of the molar heat capacities, 1.4, dimensionless |
| $\delta$ | Non-stoichiometry, dimensionless |
| $\delta^*$ | Non-stoichiometry at the equilibrium state, dimensionless |
| $\varepsilon_b$ | Bed voidage, dimensionless |
| $\eta_c$ | Compression coefficient, dimensionless |
| $\lambda_g$ | Average thermal conductivity of gas mixture, W/(m·K) |
| $\lambda_r$ | Radial heat dispersion coefficient, W/(m·K) |

$\lambda_{eff}$ Axial effective heat dispersion coefficient, W/(m·K)

$\lambda_z^0$ Static contribution to $\lambda_{eff}$, W/(m·K)

$\mu_g$ Average viscosity of gas mixture, kg/(m·s)

$\rho_b$ Bulk density of sorbents, kg/m$^3$

$\rho_g$ Average density of gas mixture, kg/m$^3$

$\rho_p$ Apparent density of pellets, kg/m$^3$

## References


[1] S.S. Hashim, A.R. Mohamed, S. Bhatia, Oxygen separation from air using ceramic-based membrane technology for sustainable fuel production and power generation, Renew. Sust. Energ. Rev. 15(2) (2011) 1284-1293. https://doi.org/10.1016/j.rser.2010.10.002.

[2] J.C. Santos, A.F. Portugal, F.D. Magalhães, A. Mendes, Optimization of Medical PSA Units for Oxygen Production, Ind. Eng. Chem. Res. 45(3) (2006) 1085-1096. https://doi.org/10.1021/ie0504809.

[3] A.R. Smith, J. Klosek, A review of air separation technologies and their integration with energy conversion processes, Fuel Process. Technol. 70(2) (2001) 115-134. https://doi.org/Doi 10.1016/S0378-3820(01)00131-X.

[4] M. Aneke, M. Wang, Potential for improving the energy efficiency of cryogenic air separation unit (ASU) using binary heat recovery cycles, Appl. Therm. Eng. 81 (2015) 223-231. https://doi.org/10.1016/j.applthermaleng.2015.02.034.

[5] Y. Kansha, A. Kishimoto, T. Nakagawa, A. Tsutsumi, A novel cryogenic air separation process based on self-heat recuperation, Sep. Purif. Technol. 77(3) (2011) 389-396. https://doi.org/10.1016/j.seppur.2011.01.012.

[6] Q. Fu, Y. Kansha, C. Song, Y. Liu, M. Ishizuka, A. Tsutsumi, A cryogenic air separation process based on self-heat recuperation for oxy-combustion plants, Appl. Energy 162 (2016) 1114-1121. https://doi.org/10.1016/j.apenergy.2015.03.039.

[7] Banaszkiewicz T, Chorowski M, Gizicki W, Comparative analysis of cryogenic and PTSA technologies for systems of oxygen production, AIP Conf. Proc. 1573 (2014) 1373-1378. https://doi.org/10.1063/1.4860866

[8] M. Mehrpooya, B. Golestani, S.M. Ali Mousavian, Novel cryogenic argon recovery from the air separation unit integrated with LNG regasification and $CO_2$ transcritical power cycle, Sustain. Energy Technol. Assess. 40 (2020). https://doi.org/10.1016/j.seta.2020.100767.

[9] M. Mofarahi, J. Towfighi, L. Fathi, Oxygen Separation from Air by Four-Bed Pressure Swing Adsorption, Ind. Eng. Chem. Res. 48(11) (2009) 5439-5444. https://doi.org/10.1021/ie801805k.

[10] X. Yang, F.E. Epiepang, J. Li, Y. Wei, Y. Liu, R.T. Yang, Sr-LSX zeolite for air separation, Chem. Eng. J. 362 (2019) 482-486. https://doi.org/10.1016/j.cej.2019.01.066.

[11] V.R. Rao, S. Farooq, W.B. Krantz, Design of a two-step pulsed pressure-swing adsorption-based oxygen concentrator, AlChE J. 56 (2009) 354-370.

https://doi.org/10.1002/aic.11953.

[12] S.U. Rege, R.T. Yang, Limits for Air Separation by Adsorption with LiX Zeolite, Ind. Eng. Chem. Res. 36(12) (1997) 5358-5365. https://doi.org/10.1021/ie9705214.

[13] M. Shi, J. Kim, J.A. Sawada, J. Lam, S. Sarabadan, T.M. Kuznicki, S.M. Kuznicki, Production of argon free oxygen by adsorptive air separation on Ag-ETS-10, AlChE J. 59(3) (2013) 982-987. https://doi.org/10.1002/aic.13879.

[14] T. Banaszkiewicz, M. Chorowski, Analysis of the applicability of adsorption oxygen generators in the field of industry and power engineering, J. Power Technol. 95 (2015) 1-5. https://papers.itc.pw.edu.pl/index.php/JPT/article/view/658.

[15] S.A. Hosseinzadeh Hejazi, L. Estupiñan Perez, A. Rajendran, S. Kuznicki, Cycle Development and Process Optimization of High-Purity Oxygen Production Using Silver-Exchanged Titanosilicates, Ind. Eng. Chem. Res. 56(19) (2017) 5679-5691. https://doi.org/10.1021/acs.iecr.7b00219.

[16] R.S. Murali, T. Sankarshana, S. Sridhar, Air Separation by Polymer-based Membrane Technology, Sep. Purif. Rev. 42(2) (2013) 130-186. https://doi.org/10.1080/15422119.2012.686000.

[17] P.N. Dyer, R.E. Richards, S.L. Russek, D.M. Taylor, Ion transport membrane technology for oxygen separation and syngas production, Solid State Ion. 134(1) (2000) 21-33. https://doi.org/https://doi.org/10.1016/S0167-2738(00)00710-4.

[18] H.S. Coombe, S. Nieh, Polymer membrane air separation performance for portable oxygen enriched combustion applications, Energy Convers. Manage. 48(5) (2007) 1499-1505. https://doi.org/10.1016/j.enconman.2006.11.021.

[19] J. Sunarso, S. Baumann, J.M. Serra, W.A. Meulenberg, S. Liu, Y.S. Lin, J.C. Diniz da Costa, Mixed ionic–electronic conducting (MIEC) ceramic-based membranes for oxygen separation, J. Membr. Sci. 320(1-2) (2008) 13-41. https://doi.org/10.1016/j.memsci.2008.03.074.

[20] I. Pfaff, A. Kather, Comparative thermodynamic analysis and integration issues of CCS steam power plants based on oxy-combustion with cryogenic or membrane based air separation, Energy Procedia 1(1) (2009) 495-502. https://doi.org/10.1016/j.egypro.2009.01.066.

[21] J. Dou, E. Krzystowczyk, A. Mishra, X. Liu, F. Li, Perovskite Promoted Mixed Cobalt–Iron Oxides for Enhanced Chemical Looping Air Separation, ACS Sustain. Chem. Eng. 6(11) (2018) 15528-15540. https://doi.org/10.1021/acssuschemeng.8b03970.

[22] B. Bulfin, J. Lapp, S. Richter, D. Gubàn, J. Vieten, S. Brendelberger, M. Roeb, C. Sattler, Air separation and selective oxygen pumping via temperature and pressure swing oxygen adsorption using a redox cycle of $SrFeO_3$ perovskite, Chem. Eng. Sci. 203 (2019) 68-75. https://doi.org/10.1016/j.ces.2019.03.057.

[23] T. Jia, J.W. Lekse, G.A. Hackett, Y. Duan, Effects of Site and Magnetic Disorder on the Oxygen Vacancy Formation and Electronic and Optical Properties of LaxSr1–xCoO3–δ and SrFeyCo1–yO3–δ, J. Phys. Chem. C 125(22) (2021) 12374-12381. https://doi.org/10.1021/acs.jpcc.1c02577.

[24] A. Sato, G. Saito, K. Abe, Y. Kunisada, N. Sakaguchi, T. Akiyama, T. Nomura, Rapid oxygen storage and release with Brownmillerite-structured Ca2AlMnO5, J. Alloys Compd. 851 (2021). https://doi.org/10.1016/j.jallcom.2020.156817.

[25] T. Jia, E.J. Popczun, J.W. Lekse, Y. Duan, The optimal co-doping of SrFe1-xCoxO3-delta oxygen carriers in redox applications, Phys. Chem. Chem. Phys. 22(29) (2020) 16721-16726. https://doi.org/10.1039/d0cp02835e.

[26] H. Zhao, K. Wang, Y. Fang, J. Ma, D. Mei, C. Zheng, Characterization of natural copper ore as oxygen carrier in chemical-looping with oxygen uncoupling of anthracite, Int. J. Greenh. Gas Control. 22 (2014) 154-164. https://doi.org/10.1016/j.ijggc.2013.12.023.

[27] K. Shah, B. Moghtaderi, J. Zanganeh, T. Wall, Integration options for novel chemical looping air separation (ICLAS) process for oxygen production in oxy-fuel coal fired power plants, Fuel 107 (2013) 356-370. https://doi.org/10.1016/j.fuel.2013.01.007.

[28] K. Wang, Q. Yu, L. Hou, Z. Zuo, Q. Qin, H. Ren, Simulation and energy consumption analysis of chemical looping air separation system on Aspen Plus, J. Therm. Anal. Calorim. 124(3) (2016) 1555-1560. https://doi.org/10.1007/s10973-016-5237-9.

[29] C. C. Cormos, Energy and cost efficient manganese chemical looping air separation cycle for decarbonized power generation based on oxy-fuel combustion and gasification, Energy 191 (2020). https://doi.org/10.1016/j.energy.2019.116579.

[30] K. Wang, Q. Yu, Q. Qin, The thermodynamic method for selecting oxygen carriers used for chemical looping air separation, J. Therm. Anal. Calorim. 112(2) (2012) 747-753. https://doi.org/10.1007/s10973-012-2596-8.

[31] B. Moghtaderi, Application of Chemical Looping Concept for Air Separation at High Temperatures†, Energy Fuels 24(1) (2010) 190-198. https://doi.org/10.1021/ef900553j.

[32] A. Fossdal, E. Bakken, B.A. Øye, C. Schøning, I. Kaus, T. Mokkelbost, Y. Larring, Study of inexpensive oxygen carriers for chemical looping combustion, Int. J. Greenh. Gas Control. 5(3) (2011) 483-488. https://doi.org/10.1016/j.ijggc.2010.08.001.

[33] J. Vieten, B. Bulfin, P. Huck, M. Horton, D. Guban, L. Zhu, Y. Lu, K.A. Persson, M. Roeb, C. Sattler, Materials design of perovskite solid solutions for thermochemical applications, Energy Environ. Sci. 12(4) (2019) 1369-1384. https://doi.org/10.1039/c9ee00085b.

[34] A. Lyngfelt, Chemical-looping combustion of solid fuels – Status of development, Appl. Energy 113 (2014) 1869-1873. https://doi.org/10.1016/j.apenergy.2013.05.043.

[35] X. Zhu, F. Donat, Q. Imtiaz, C.R. Müller, F. Li, Chemical Looping Beyond Combustion – A Perspective, Energy Environ. Sci. 13(3) (2020) 772-804. https://doi.org/10.1039/c9ee03793d.

[36] M. Su, J. Cao, X. Tian, Y. Zhang, H. Zhao, Mechanism and kinetics of Cu2O oxidation in chemical looping with oxygen uncoupling, Proc. Combust. Inst. 37(4) (2019) 4371-4378. https://doi.org/10.1016/j.proci.2018.06.162.

[37] G. Luongo, F. Donat, C.R. Muller, Structural and thermodynamic study of Ca A- or Co B-site substituted $SrFeO_{3-\delta}$ perovskites for low temperature chemical looping applications, Phys. Chem. Chem. Phys. 22(17) (2020) 9272-9282. https://doi.org/10.1039/d0cp01049a.

[38] X. Tian, Y. Wei, H. Zhao, Using a hierarchically-structured $CuO@TiO_2$-$Al_2O_3$ oxygen carrier for chemical looping air separation in a paralleled fluidized bed reactor, Chem. Eng. J. 334 (2018) 611-618. https://doi.org/10.1016/j.cej.2017.10.084.

[39] H. Song, K. Shah, E. Doroodchi, B. Moghtaderi, Development of a Cu–Mg-Based Oxygen Carrier with $SiO_2$ as a Support for Chemical Looping Air Separation, Energy Fuels 28(1) (2013) 163-172. https://doi.org/10.1021/ef401485p.

[40] N. Galinsky, M. Sendi, L. Bowers, F. Li, $CaMn_{1-x}B_xO_{3-\delta}$ (B = Al, V, Fe, Co, and Ni) perovskite based oxygen carriers for chemical looping with oxygen uncoupling (CLOU), Appl. Energy 174 (2016) 80-87. https://doi.org/10.1016/j.apenergy.2016.04.046.

[41] R.H. Görke, W. Hu, M.T. Dunstan, J.S. Dennis, S.A. Scott, Exploration of the material property space for chemical looping air separation applied to carbon capture and storage, Appl. Energy 212 (2018) 478-488. https://doi.org/10.1016/j.apenergy.2017.11.083.

[42] E. Krzystowczyk, X. Wang, J. Dou, V. Haribal, F. Li, Substituted $SrFeO_3$ as robust oxygen sorbents for thermochemical air separation: correlating redox performance with compositional and structural properties, Phys. Chem. Chem. Phys. 22(16) (2020) 8924-8932. https://doi.org/10.1039/d0cp00275e.

[43] H. C. Wu, Y.S. Lin, Effects of Oxygen Vacancy Order–Disorder Phase Transition on Air Separation by Perovskite Sorbents, Ind. Eng. Chem. Res. 56(20) (2017) 6057-6064. https://doi.org/10.1021/acs.iecr.7b00461.

[44] H. Ding, Y. Xu, C. Luo, Q. Wang, S. Li, G. Cai, L. Zhang, Y. Zheng, Q. Shen, Oxygen desorption behavior of sol-gel derived perovskite-type oxides in a pressurized fixed bed reactor, Chem. Eng. J. 323 (2017) 340-346. https://doi.org/10.1016/j.cej.2017.04.100.

[45] J. Dou, E. Krzystowczyk, X. Wang, T. Robbins, L. Ma, X. Liu, F. Li, A- and B-site Codoped $SrFeO_3$ Oxygen Sorbents for Enhanced Chemical Looping Air Separation, ChemSusChem 13(2) (2020) 385-393. https://doi.org/10.1002/cssc.201902698.

[46] X. Wang, E. Krzystowczyk, J. Dou, F. Li, Net Electronic Charge as an Effective Electronic Descriptor for Oxygen Release and Transport Properties of $SrFeO_3$-Based Oxygen Sorbents, Chem. Mater. 33(7) (2021) 2446-2456. https://doi.org/10.1021/acs.chemmater.0c04658.

[47] E.J. Popczun, T. Jia, S. Natesakhawat, C.M. Marin, T.D. Nguyen-Phan, Y. Duan, J.W. Lekse, Investigation of Sr0.7 Ca0.3 FeO3 Oxygen Carriers with Variable Cobalt B-Site Substitution, ChemSusChem 14(8) (2021) 1893-1901. https://doi.org/10.1002/cssc.202002849.

[48] Z. Deng, B. Jin, Y. Zhao, H. Gao, Y. Huang, X. Luo, Z. Liang, Process simulation and thermodynamic evaluation for chemical looping air separation using fluidized bed reactors, Energy Convers. Manage. 160 (2018) 289-301. https://doi.org/10.1016/j.enconman.2018.01.039.

[49] R.J. Lee Pereira, P.A. Argyris, V. Spallina, A comparative study on clean ammonia production using chemical looping based technology, Appl. Energy 280 (2020). https://doi.org/10.1016/j.apenergy.2020.115874.

[50] B. Bulfin, J. Vieten, S. Richter, J.M. Naik, G.R. Patzke, M. Roeb, C. Sattler, A. Steinfeld, Isothermal relaxation kinetics for the reduction and oxidation of $SrFeO_3$ based perovskites, Phys. Chem. Chem. Phys. 22(4) (2020) 2466-2474. https://doi.org/10.1039/c9cp05771d.

[51] S.A. Hosseinzadeh Hejazi, L. Estupiñan Perez, A. Rajendran, S. Kuznicki, Cycle Development and Process Optimization of High-Purity Oxygen Production Using Silver-Exchanged Titanosilicates, Ind. Eng. Chem. Res. 56(19) (2017) 5679-5691. https://doi.org/10.1021/acs.iecr.7b00219.

[52] S.A. Hosseinzadeh Hejazi, L. Estupiñan Perez, A. Rajendran, S. Kuznicki, Cycle Development and Process Optimization of High-Purity Oxygen Production Using Silver-Exchanged Titanosilicates, Ind. Eng. Chem. Res. 56(19) (2017) 5679-5691.

https://doi.org/10.1021/acs.iecr.7b00219.

[53] X. Yang, H. Wang, J. Chen, Z. Li, Y. Liu, C. Zhang, Y. Xing, Two-Dimensional Modeling of Pressure Swing Adsorption (PSA) Oxygen Generation with Radial-Flow Adsorber, Appl. Sci. 9(6) (2019). https://doi.org/10.3390/app9061153.

[54] M. Xu, H.-C. Wu, Y.S. Lin, S. Deng, Simulation and optimization of pressure swing adsorption process for high-temperature air separation by perovskite sorbents, Chem. Eng. J. 354 (2018) 62-74. https://doi.org/10.1016/j.cej.2018.07.080.

[55] J. Dou, E. Krzystowczyk, X. Wang, A.R. Richard, T. Robbins, F. Li, $Sr_{1-x}Ca_xFe_{1-y}Co_yO_{3-\delta}$ as facile and tunable oxygen sorbents for chemical looping air separation, J. Phys. Energy 2(2) (2020) 025007. https://doi.org/10.1088/2515-7655/ab7cb0.

[56] L. Ge, Z. Zhu, Z. Shao, S. Wang, S. Liu, Effects of preparation methods on the oxygen non-stoichiometry, B-site cation valences and catalytic efficiency of perovskite La0.6Sr0.4Co0.2Fe0.8O3−δ, Ceram. Int. 35(8) (2009) 3201-3206. https://doi.org/10.1016/j.ceramint.2009.05.024.

[57] B. Sankararao, S.K. Gupta, Multi-Objective Optimization of Pressure Swing Adsorbers for Air Separation, Ind. Eng. Chem. Res. 46(11) (2007) 3751-3765. https://doi.org/10.1021/ie0615180.

[58] A. M. M. Mendes, C.A.V. Costa, A.r.E. Rodrigues, Oxygen separation from air by PSA: modelling and experimental results: Part I: isothermal operation, Sep. Purif. Technol. 24(1) (2001) 173-188. https://doi.org/https://doi.org/10.1016/S1383-5866(00)00227-6.

[59] P. E. Jahromi, S. Fatemi, A. Vatani, J.A. Ritter, A.D. Ebner, Purification of helium from a cryogenic natural gas nitrogen rejection unit by pressure swing adsorption, Sep. Purif. Technol. 193 (2018) 91-102. https://doi.org/10.1016/j.seppur.2017.11.002.

[60] L. Han, Z. Zhou, G.M. Bollas, Heterogeneous modeling of chemical-looping combustion. Part 1: Reactor model, Chem. Eng. Sci. 104 (2013) 233-249. https://doi.org/10.1016/j.ces.2013.09.021.

[61] N.A.A. Qasem, R. Ben-Mansour, Energy and productivity efficient vacuum pressure swing adsorption process to separate $CO_2$ from $CO_2/N_2$ mixture using Mg-MOF-74: A CFD simulation, Appl. Energy 209 (2018) 190-202. https://doi.org/10.1016/j.apenergy.2017.10.098.

[62] J.-G. Jee, J.-S. Lee, C.-H. Lee, Air Separation by a Small-Scale Two-Bed Medical $O_2$ Pressure Swing Adsorption, Ind. Eng. Chem. Res. 40(16) (2001) 3647-3658. https://doi.org/10.1021/ie010101l.

[63] Y. He, X. Zhu, Q. Li, W. Yang, Perovskite oxide absorbents for oxygen separation, AlChE J. 55(12) (2009) 3125-3133. https://doi.org/10.1002/aic.11931.

[64] P. Hao, Y. Shi, S. Li, S. Liang, Oxygen sorption/desorption kinetics of $SrCo_{0.8}Fe_{0.2}O_{3-\delta}$ perovskite adsorbent for high temperature air separation, Adsorption 24(1) (2017) 65-71. https://doi.org/10.1007/s10450-017-9922-1.

[65] R.H. Görke, E.J. Marek, F. Donat, S.A. Scott, Reduction and oxidation behavior of strontium perovskites for chemical looping air separation, Int. J. Greenh. Gas Control. 94 (2020). https://doi.org/10.1016/j.ijggc.2019.102891.

[66] B. Bulfin, J. Vieten, S. Richter, J.M. Naik, G.R. Patzke, M. Roeb, C. Sattler, A. Steinfeld, Isothermal relaxation kinetics for the reduction and oxidation of $SrFeO_3$ based perovskites, Phys. Chem. Chem. Phys. 22(4) (2020) 2466-2474.

https://doi.org/10.1039/c9cp05771d.

[67] M.F. Edwards, J.F. Richardson, Gas dispersion in packed beds, Chem. Eng. Sci. 23(2) (1968) 109-123. https://doi.org/https://doi.org/10.1016/0009-2509(68)87056-3.

[68] C. Haavik, E. Bakken, T. Norby, S. Stølen, T. Atake, T. Tojo, Heat capacity of $SrFeO_{3-\delta}$; $\delta$ = 0.50, 0.25 and 0.15 – configurational entropy of structural entities in grossly non-stoichiometric oxides, Dalton Trans. (3) (2003) 361-368. https://doi.org/10.1039/b209236k.

[69] Y. Hao, C.-K. Yang, S.M. Haile, Ceria–Zirconia Solid Solutions ($Ce_{1-x}Zr_xO_{2-\delta}$, $x \leq 0.2$) for Solar Thermochemical Water Splitting: A Thermodynamic Study, Chem. Mater. 26(20) (2014) 6073-6082. https://doi.org/10.1021/cm503131p.

[70] D. Ko, R. Siriwardane, L.T. Biegler, Optimization of Pressure Swing Adsorption and Fractionated Vacuum Pressure Swing Adsorption Processes for $CO_2$ Capture, Ind. Eng. Chem. Res. 44(21) (2005) 8084-8094. https://doi.org/10.1021/ie050012z.

[71] E. Krzystowczyk, V. Haribal, J. Dou, F. Li, Chemical Looping Air Separation Using A Perovskite Based Oxygen Sorbent – System Design and Process Analysis, 2021, ACS Sustainable Chemistry & Engineering (In press).

[72] D.K. Khosla, S.K. Gupta, D.N. Saraf, Multi-objective optimization of fuel oil blending using the jumping gene adaptation of genetic algorithm, Fuel Process. Technol. 88(1) (2007) 51-63. https://doi.org/10.1016/j.fuproc.2006.08.009.

[73] N. Agrawal, G.P. Rangaiah, A.K. Ray, S.K. Gupta, Design stage optimization of an industrial low-density polyethylene tubular reactor for multiple objectives using NSGA-II and its jumping gene adaptations, Chem. Eng. Sci. 62(9) (2007) 2346-2365. https://doi.org/10.1016/j.ces.2007.01.030.

[74] T. Banaszkiewicz, M. Chorowski, Energy consumption of air-separation adsorption methods, Entropy (Basel) 20(4) (2018). https://doi.org/10.3390/e20040232.

[75] S.W. Chai, M.V. Kothare, S. Sircar, Rapid pressure swing adsorption for reduction of bed size factor of a medical oxygen concentrator, Ind. Eng. Chem. Res. 50(14) (2011) 8703-8710. https://doi.org/10.1021/ie2005093.

[76] C. Tian, Q. Fu, Z. Ding, Z. Han, D. Zhang, Experiment and simulation study of a dual-reflux pressure swing adsorption process for separating N2/O2, Sep. Purif. Technol. 189 (2017) 54-65. https://doi.org/10.1016/j.seppur.2017.06.041.